Mechanically robust nitrogen-rich plasma polymers: Biofunctional interfaces for surface engineering of biomedical implants

Omid Sharifahmadian [a, b], Chongpu Zhai [c, d], Juichien Hung [e], Ghazal Shineh [f], Callum A.C. Stewart [a], Arifah A. Fadzil [a, f], Mihail Ionescu [g], Yixiang Gan [c], Steven G. Wise [e, h, i], Behnam Akhavan [a, f, h, *]

[a] School of Physics, University of Sydney, Sydney, New South Wales 2006, Australia
[b] Coating Department, Centre for Functional and Surface Functionalised Glass, Alexander Dubcek University of Trencin, 91150 Trencin, Slovakia
[c] School of Civil Engineering, University of Sydney, Sydney, New South Wales 2006, Australia
[d] State Key Laboratory for Strength and Vibration of Mechanical Structures, School of Aerospace, Xi'an Jiaotong University, Xi'an, 710049, China
[e] Department of Physiology, School of Medical Sciences, University of Sydney, Sydney, New South Wales 2006, Australia
[f] School of Biomedical Engineering, University of Sydney, Sydney, New South Wales 2006, Australia
[g] Australian Nuclear Science and Technology Organisation, New Illawarra Rd, Sydney, NSW 2234, Australia
[h] Sydney Nano Institute, the University of Sydney, Camperdown, Sydney, New South Wales 2006, Australia
[i] Charles Perkins Centre, University of Sydney, Sydney, New South Wales 2006, Australia

ARTICLE INFO

ABSTRACT

Surface bio-functionalization through covalent attachment of bioactive molecules is a promising approach to facilitate rapid bone-implant integration. Radical-rich plasma polymer interlayers are highly attractive as platforms that enable covalent biofunctionalization in a single-step, reagent-free manner. However, fabrication of mechanically robust plasma polymer films, particularly for biomedical devices that operate in corrosive body fluids, is not trivial. Here we show a facile approach to tune the robustness of ion-assisted plasma polymer (IPP) films via simply varying the nitrogen atomic concentration incorporated into their structure. X-ray photoelectron spectroscopy data indicated that the total sp^3/sp^2 ratio of carbon atoms decreases in the films with increasing nitrogen atomic concentration. Electron recoil detection analysis data provided evidence that the hydrogen content decreases as the nitrogen atomic concentration increases. Nano-indentation and nano-scratch tests, together with long-term stability studies in simulated body fluid, showed a strong correlation between the nitrogen atomic concentration and the robustness and stability of the films. We confirmed the potential of the optimized, nitrogen-rich IPP film to regulate osseointegration by covalent attachment of fibronectin followed by quantifying primary osteoblast attachment and proliferation. The IPP films developed here hold great potential as robust interfaces for biomimetic surface engineering of implantable biomedical devices, in particular bone implants.

1. Introduction

Rising incidences of bone diseases such as osteoporosis and cancer as well as increasing cases of bone fractures in rapidly aging populations have increased the demand for bone implants. In the United States alone, for example, an increase of 174% for total hip arthroplasty and an increase of 673% for total knee arthroplasty by 2030 have been predicted [1]. Despite recent advances in surgical techniques and designs of prostheses, implant failure is still significant, particularly in patients with poor bone quality and chronic medical conditions [2].

Post-operative complications and the failure of bone implants are primarily due to weak integration of implants with host tissue or bacterial infection [3,4]. If left untreated, surfaces of metallic implants, such as titanium-based alloys, are not capable of providing biological cues to promote tissue integration. This lack of biofunctionality leaves bone-tissue integration to compete with adverse responses such as inflammation and infection, which

* Corresponding author. School of Physics, University of Sydney, Sydney, New South Wales 2006, Australia.
E-mail address: behnam.akhavan@sydney.edu.au (B. Akhavan).

eventually lead to aseptic loosening and implant failure [5,6].

Surface engineering of bone implants is a viable approach to reduce their failure by encouraging their integration with the local bone tissue and reducing the chances of foreign body reaction induced fibrosis and infection. In recent years, significant research has been carried out on surface modification of titanium-based alloys for enhanced osseointegration. The techniques that have been used in this domain include physicochemical surface treatments [6,7], grit-blasting [8], electrochemical modification [9,10], laser surface modification [11], and surface bio-functionalization [12]. Among these approaches, surface biofunctionalization using bioactive molecules such as proteins and peptides has gained particular interest as a strategy with great potential [3]. Biofunctionalization of implant surfaces allows for mimicking osseointegration stimulating cues of the surrounding host tissue and thus encouraging more rapid bone integration.

Surface biofunctionalization is typically achieved either through simple physical adsorption [13] or covalent immobilization using chemical linkers or other reagents [14]. The physical adsorption approach is not suitable for real-world implant applications, due to the desorption of physisorbed biomolecules or their competitive replacement by other molecules *in vivo* [3]. This problem can be overcome using multi-step immobilization strategies based on wet chemical reactions using chemical linkers or other reagents, which are not easy to control due to the potential for side reactions. These techniques are also often time-consuming, cumbersome, and substrate-dependent; thus, making them challenging for scale-up. The extensive usage of solvents and reagents in these methods also introduces problems in waste disposal and obtaining regulatory approvals [15,16].

We have recently developed a novel plasma-based technology for direct covalent attachment of a wide range of biomolecules, such as antimicrobial and antifungal peptides [17], silver nanoparticles [18], bone morphogenic protein-2 (BMP2) [19], and a multifunctional fusion protein, combining the fibronectin (FN) attachment and osteocalcin (OCN) bone signalling sequences [20] on titanium surfaces. This strategy relies on generating a radical-functionalized plasma polymer layer through a combination of plasma polymerization and plasma immersion ion implantation. In this process, the metallic substrates, such as titanium, are negatively biased in a pulsed manner as the plasma polymer film grows. This strategy enables the formation of a large concentration of reactive radicals embedded within the ion-assisted plasma polymer (IPP) structure. The mobile radicals migrate to the IPP surface over time and form covalent bonds with almost any biomolecule that becomes in contact with the surface [21,22]. The biofunctionalization of such radical-rich interlayers is simple as it can be carried out in a single-step at room temperature. Unlike the traditional wet-chemistry methods, this approach doesn't require a sequence of wet-chemistry steps or any other chemical reagents to achieve covalent surface biofunctionalization [3]. Another advantage of this approach is that the reagent-and-linker-free mechanism of covalent attachment provides the opportunity of tuning the orientation and density of small biomolecules such as peptides on the surface. This is achieved simply by either tuning the pH of the biomolecule solution to manipulate the double-layer at the surface or applying external electric fields using small power supplies or household batteries [23].

The mechanical stability of IPP films are particularly important for bone implantable devices as the film must tolerate the mechanical stresses encountered during aggressive surgical insertion and normal use *in vivo*. Mechanical stability of a thin film is controlled by both interfacial adhesion to the substrate and degree of internal stress [24,25]. However, achieving mechanically robust films that exhibit strong adhesion to the substrate with minimal internal stress remains an on-going, multifaceted challenge in the field.

We have recently demonstrated that the enhanced ion bombardment during the early stage of ion-assisted plasma polymerization regulates the mechanism of film growth at the interface. Therefore, it can play a critical role in increasing the adhesion of the plasma polymerized film to carbide-forming substrates such as titanium and zirconium [19,26] and also induces atomic interface mixing for non-carbide forming materials to create a stronger interface. Such interface engineering through regulating the ion bombardment has great potential for enhancing the film-substrate adhesion. However, the compressive residual stress of the subsequently grown films also needs to be controlled to optimise resistance to delamination. The residual stress of organic thin films can be modulated by changing their chemical composition. For example, the incorporation of elements such as nitrogen [27], silicon [28,29], fluorine [30] and chromium [31] has been shown to reduce the residual internal stress in a-C:H films. It has been well documented in the literature that the reduction of residual internal stress by increasing the concentration of these elements is related to structural transformations from sp^3-like to sp^2-like carbon bonding [32,33]. In particular, the influence of nitrogen doping on the residual internal stress has been investigated for thin films produced using pulse laser deposition [34], ion beam deposition [35] and filtered cathodic arc [36].

Here we report a simple approach to create highly stable IPP films for covalent biofunctionalziation of implantable devices by simply tuning the nitrogen atomic concentration incorporated in the film's structure. We elucidate the role of nitrogen in regulating the growth mechanisms and in physicochemical structure of the IPP films. We provide evidence that by optimizing this structure, highly robust polymeric interfaces that withstand failure in simulated body fluids for at least two months, even after being scratched or mechanically deformed, are achieved. Further, we demonstrated the excellent capability of the optimized IPP film to covalently tether fibronectin (FN), as a model biomolecule, and examined the responses of primary osteoblast cells to films with various concentrations of nitrogen. Primary osteoblast attachment and proliferation are also quantified on uncoated IPP films as well as following covalent immobilization of fibronectin. The findings reported in this paper hold great potential to open up new avenues of research on surface biofunctionazlaition of metallic biomaterials for eliciting optimal biological responses from implantable biomedical devices for accelerated integration with host tissues.

2. Experimental section

2.1. Materials and reagents

Titanium foils (Firmetal, China) and boron doped, p-type silicon wafers (University Wafers) were used as substrates. High-purity acetylene (C_2H_2), nitrogen (N_2), and argon (Ar) gases were obtained from BOC Australia and used for ion-assisted plasma polymerization. Sodium dodecylsulfate (SDS), bovine serum albumin (BSA) and fibronectin from human plasma were obtained from Sigma-Aldrich. Primary osteoblasts from adult mouse long bones were harvested from (6–8)-week old C57BL/6 mice according to a standard protocol [37].

2.2. Ion-assisted plasma polymerization

A custom-built ion-assisted plasma polymerization system, schematically illustrated in Fig. 1, was used to deposit ion-assisted plasma polymers containing various concentrations of nitrogen. The plasma system was equipped with an RF power supply (ENI;
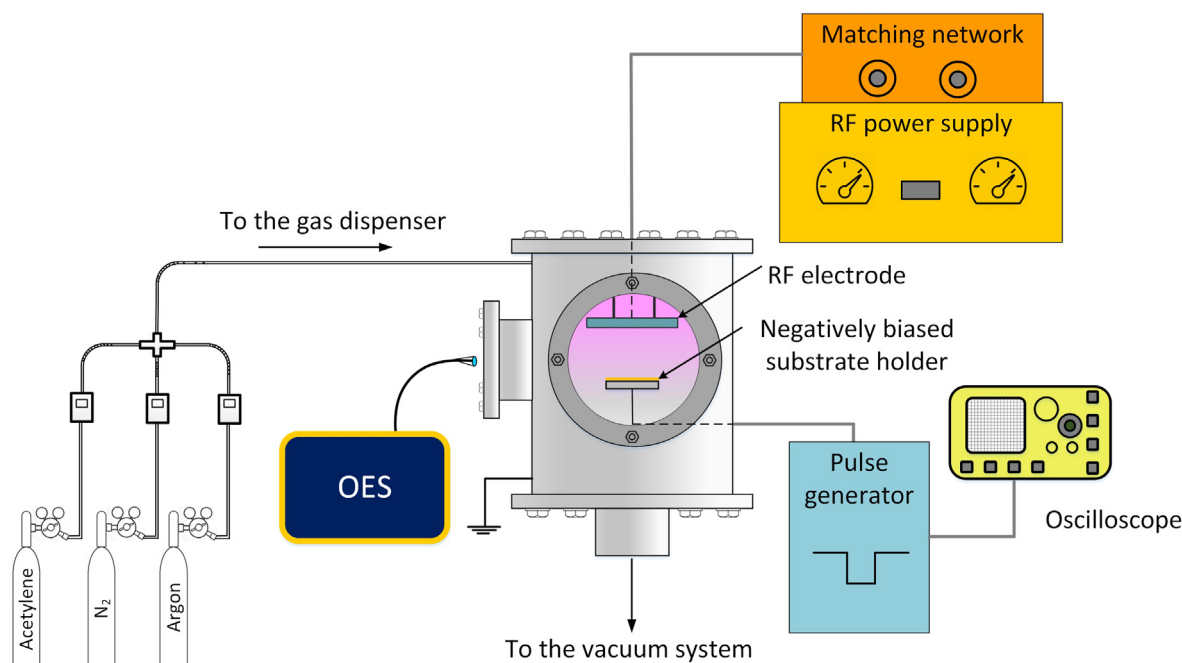
Fig. 1. Schematic diagram showing the configuration of the ion-assisted plasma polymerization system used for the deposition of radical-functionalized coatings.

OEM-6AM-1) and a RUP6 pulsed DC power source (GBS-Electronik) connected to the top electrode and substrate holder, respectively. This system has previously been described in detail [17,19]. The substrates were initially sonicated for 10 min in acetone and ethanol each and were then cleaned by argon plasma for 10 min using an argon flow rate of 40 standard cubic centimetres per minute (sccm), RF power of 75 W, and pulsed substrate bias voltage of - 500 V with a pulse width of 20 μs, applied at a frequency of 3 kHz. Various N_2/C_2H_2 flow rate ratios of 0, 0.5, 1, 2, and 5 and a constant flow rate of argon (15 sccm), at a working pressure of 110 mTorr, were applied for the deposition of IPP coatings. Corresponding C_2H_2 and N_2 flow rates for each ratio are listed in Table 1. The depositions were carried out using an RF power of 50 W, and a pulsed bias voltage of -500 V with a pulse width of 20 μs, applied at a frequency of 3 kHz. The base pressure for all deposition runs was below 5×10^{-2} mTorr. The deposition times were adjusted to achieve a constant thickness of ~30 nm for IPP coatings deposited using the various N_2/C_2H_2 ratios.

2.3. Optical emission spectroscopy (OES)

The synthesis of IPP coatings using various N_2/C_2H_2 flow rate ratios was monitored in-situ using OES. The OES spectra were obtained utilizing an Acton Spectra Pro 2750 spectrometer (Princeton Instruments, USA). The spectrometer, equipped with a 1200 grooves mm^{-1} grating, had a nominal resolution of 0.014 nm for an

Table 1
The range of N_2/C_2H_2 flow rate ratios used for ion-assisted plasma polymer depositions to produce coatings with various concentrations of nitrogen.

N_2/C_2H_2 Flow rate ratio	C_2H_2 Flow rate (sccm)	N_2 Flow rate (sccm)
0	10	0
0.5	10	5
1	7.5	7.5
2	5	10
5	2.5	12.5

entrance slit opening of 50 μm. An intensified charge-coupled device (ICCD) was used to capture the emission spectra (1024 × 1024 pixel array) from the discharges at an exposure time of 300 μs. To improve the signal-to-noise ratio, 150 consecutive acquisitions were averaged. The optical setups were kept unchanged for all the measurements.

2.4. X-ray photoelectron spectroscopy (XPS)

To analyze the surface chemistry of the IPP films deposited on Ti substrates, a FlexMode SPECS spectrometer was used. The XPS system was equipped with a mono chromatic Al Kα radiation source (hv = 1486.7 eV), an MCD9 electron detector, and a hemispherical analyzer (PHOIBOS 150). All the XPS measurements were conducted within 1 h after ion-assisted plasma polymerization. The X-ray source operated at 200 W with a voltage of 10 kV and current of 20 mA. The pressure during the measurements was at least 5.0×10^{-8} mbar. The electron take-off angle was 90° for the acquisition of survey and high resolution spectra. The survey spectra were obtained at a resolution of 0.5 eV (energy range of 0−1000 eV) and a pass energy of 30 eV. The carbon (C 1s) and nitrogen (N 1s) high resolution spectra (pass energy = 20 eV) were collected at a resolution of 0.1 eV. Identical full-width at half-maximum (FWHM) values were applied for peak fitting of high resolution spectra, while a linear background and line shapes of Gaussian (70%) and Lorentzian (30%) were used. Casa XPS software (Version 2.3.14) was used for elemental composition calculations and peak fitting of spectra.

2.5. Attenuated total reflectance Fourier transform infrared spectroscopy (ATR-FTIR)

The ATR-FTIR spectra from the IPP coatings with various nitrogen atomic concentrations, deposited on the Ti substrates, were obtained using a Digilab FTS7000 FTIR. The FTIR device was coupled with an ATR accessory (Harrick, USA). A trapezium germanium crystal (width = 1 cm) at an incident angle of 45° was used to

collect the spectra. An average of 500 scans, at a resolution of 4 cm^{-1} (in the wavelength range of 4000−850 cm^{-1}) was recorded for each sample. The dimensions of Ti substrates used for these measurements were 2 cm × 1.5 cm to ensure full coverage of the ATR crystal. Resolutions Pro software (Digilab, V. 4.0) was utilized for all the data analyses and subtraction of spectra.

2.6. Time of flight secondary ion mass spectrometry (ToF-SIMS)

ToF-SIMS was carried out using a nano TOF equipment (PHI TRIFT V, Chanhassen, MN) that was operated at 30 eV with a pulsed liquid (79Au$^+$) metal primary ion source (LMIG). All measurements were carried out in the positive mode of SIMS at base pressures below 5 × 10^{-6} Pa. Dual charge neutralization was achieved for the measurement with the aid of an electron flood gun and Ar$^+$ ions (10 eV). The data were collected for n > 6 spots for each sample, each with measurement areas of 100 μm × 100 μm. All spectra analyses were performed using WincadenceN software (version 1.8.1, Physical Electronics).

2.7. Elastic recoil detection analysis (ERDA)

The ERDA technique was employed to measure the depth profiles of hydrogen in IPP coatings on ANSTO STAR accelerator. The IPP-coated silicon wafers were exposed to a 2 MeV He beam, incident to the sample at 76° relative to the sample normal, and the detection of recoiled hydrogen atoms was measured at 152° relative to the He beam direction, using a solid state detector in a vacuum chamber at a pressure of 5 × 10−5 Pa. The total number of He ions impinging on the IPP-coated samples during measurement was monitored by integrating the beam current, and the hydrogen depth profile was obtained from the energy of recoils provided by the solid state detector, and calculated from first principles.

2.8. Nano-indentation and nano-scratch tests

An Agilent-G200 nano-indenter was used to measure the scratch responses as well as the elastic moduli of the IPP films deposited on titanium substrates. The partial unloading approach in nano-indentation (Berkovich, Synton-MDP, XP/Berkovich/020) was utilized to investigate the normal elastic responses of the samples. After each unloading step (load reducing by 20%), the loading level increased (by a factor of two to the next unloading step) up to 50 mN. By averaging over 20 tests at various points on each specimen, the stiffness values were obtained. The nano-scratch tests (conical tip, Synton-MDP, XP/Con060/005/020) were performed at a velocity of 0.25 m/s for a distance of 200 μm (with maximum normal load of 50 mN) for 10 tests on each sample.

2.9. Stability in simulated body fluid (SBF)

The stability of the IPP coatings was assessed followed by their incubation for up to 2 months in 10 mL of Tyrode's simulated body fluid (SBF) at (37 ± 1)^o C. The chemical composition of the Tyrode's solution has been reported before [26]. Within 24 h after deposition, the IPP-coated surfaces were immersed in SBF. To evaluate the coatings' stability in situations where they are also physically damaged, the samples were scratched with the shape of a cross using a sharp, high-speed steel tip prior to their incubation in the SBF solution.

2.10. Scanning electron microscopy (SEM)

IPP-coated Ti samples, before and after being stored in the SBF, were examined for possible signs of physical failure using a FEI Quanta microscope in the secondary electron (SE) mode. The samples were mounted on the sample holder using conductive carbon tape. The imaging was carried out at a chamber pressure of below 6.5 × 10^{-6} Torr. The acceleration voltage and working distance were 5 kV and 5−10 mm, respectively.

2.11. Spectroscopic ellipsometry

To determine the differences in the cross-linking degrees of IPP films deposited using various N$_2$/C$_2$H$_2$ ratios, spectroscopic ellipsometry was used to measured their refractive indices. A Woollam M2000 V spectroscopic ellipsometer equipped with an XLS-100 light source and a control module (EC-400) with WVASE32 software was utilized for these measurements. To minimise the effect of surface roughness on ellipsometry data, we used atomically smooth silicon wafers as substrates for these measurements. The analyses were carried out on IPP-coated silicon wafers at 65, 70, and 75° angles of incidence in a spectral region ranging from 200 to 1000 nm with 5 nm steps. A Cauchy layer was employed in the model to fit of the data until model convergence was achieved. The average values of refractive indices (at 630 nm) for n ≥ 3 measurements per sample were reported.

2.12. Contact angle measurements and surface free energy calculations

Water and diiodomethane contact angle measurements were carried out using a Biolin Scientific optical goniometer with One Attention software. To calculate the surface free energy of the IPP coatings and the polar and dispersive components, at least five measurements for water and diiodomethane contact angles were performed. The liquid drops with a volume of 1 μL were placed on the surfaces within 30 min after the IPP deposition and static contact angles were then measured. The Owens-Wendt model was used to calculate the surface free energy and its components using contact angles as an average of at least five measurements per sample.

2.13. Electron paramagnetic resonance (EPR) spectroscopy

The radical content of the IPP coating deposited on a polystyrene film was compared to the uncoated substrate using a Bruker EMXplus Xband. The films with dimensions of 7 cm × 7 cm were rolled tightly and placed inside a Wilmad Borosilicate glass NMR tube for the measurements. The EPR spectra were recorded with the following parameters: microwave frequency of 9.8 GHz, power of 25 mW, a central magnetic field of 3510 G, and modulation amplitude of 3 G. Ten scans were acquired for each sample and the averaged spectra are reported.

2.14. Covalent attachment of protein

Fibronectin (FN) was dissolved in PBS buffer at a concentration of 10 μg/mL. The uncoated and IPP-coated Ti substrates were incubated in the solution overnight at 4 °C and washed with excess PBS. Samples were then washed with 5% sodium dodecyl sulfate (SDS) (15 min at 90 °C) to demonstrate the covalent anchorage of FN to the IPP-coated surfaces.

2.15. Enzyme-linked immunosorbent assay (ELISA)

ELISA was used to detect surface-bound fibronectin on uncoated and IPP-coated Ti surfaces before and after SDS washing. The protein-incubated surfaces were initially immersed in 5% BSA solution followed by the application of fibronectin rabbit-anti human primary (Ab2413, Abcam; 1:5000 dilution) and a goat-anti rabbit secondary antibody (ab6721; 1:20000 dilution). The incubation time for each of these three steps was 1 h. The samples were then incubated in 1-Step Ultra TMB - ELISA Substrate (cat. 34028B, Thermofisher Scientific) for 30 min before 0.02 M sulfuric acid was added to stop the reaction. The absorbance of samples at 450 nm was measured (150 μL aliquots) using a plate reader. The ELISA assay was carried out on 3 samples per ion-assisted polymerization condition.

2.16. Osteoblast isolation and culture

Primary osteoblasts were isolated as we have previously described [19]. Experiments were conducted in accordance with the Australian Code of Practice for the Care and Use of Animals for Scientific Purpose. All personnel involved in the animal procedures have completed an approved animal care and ethics course. Mice used for primary cell harvest were surplus to approved protocols and collected for this study after they had been culled. To study the attachment of cells, osteoblasts (OB, passage 3−5, 2×10^4 cells/well) were incubated with uncoated and IPP-coated Ti surfaces for 1 h. Following this, the surfaces were washed with PBS and the cells were fixed with 70% ethanol for 10 min. The uncoated and IPP-coated samples were mounted with 4′,6-diamidino-2-phenylindole (DAPI) fluoroshield mounting medium (Sigma Aldrich). Images were collected from 4 fields, ensuring the entire surfaces of the sample are covered, and using Image J software the cell nuclei were counted. To study the proliferation of cells, OBs with a density of 4×10^3 cells/well were incubated with the uncoated and IPP-coated Ti surfaces for 3, 6, and 12 days. The media was changed every second day. MTS cell proliferation assay kit (Promega) was used to measure the metabolic activity. For this assay, 40 μl of the MTS reagent was added to each well, followed by further incubation for 2 h. The absorbance at 490 nm from formazan dye produced by viable cells was quantified. The experiments were carried out on 4 samples per ion-assisted polymerization condition, and they were repeated 3 times to ensure reproducibility. The data obtained from one representative experiment are presented.

2.17. Statistical analysis

GraphPad Prism version 7.02 was employed to compare the data shown as mean ± standard error of the mean (SEM). Comparison between data was carried out using one-way ANOVA analysis of variance (Tukey's multiple comparison groups). Statistical significance is indicated in figures as * p<0.05, **p<0.01 and ***p<0.001.

3. Results and discussion

3.1. OES diagnostics of IPP plasma discharges

To study the influence of nitrogen on the microstructural properties of the IPP films as well as their nano mechanical performance and physico-chemical stability in simulated body fluids, we changed the ratio of nitrogen to acetylene in the precursor gas mixture from 0 to 5, while keeping all the other parameters unchanged. The chemical species present in the plasma phase were diagnosed using OES in the wavelength range of 300−450 nm for various N_2/C_2H_2 ratios, and the results are shown in Fig. 2. The emission peaks associated with nitrogen/carbon ions and neutrals [38−41] were observed from the OES spectra. The spectrum obtained for the nitrogen-free plasma gas mixture ($N_2/C_2H_2 = 0$) did not show any peaks associated with nitrogen. However, increasing the flow of nitrogen present in the precursor gas mixture intensified the nitrogen-associated peaks such as CN, N_2, and N^+, and decreased the relative intensity of carbon-associated peaks such as CH. These changes are due to the increased availability of nitrogen in the plasma gas mixtures with higher N_2/C_2H_2 ratios.

The increase in the intensity ratio of CN/N_2 peaks by increasing the nitrogen concentration in the discharge is of particular interest. The emission intensity of CN radical molecules (at 388.4 nm) normalized to that of N_2 (at 380.5 nm) for the discharge with N_2/C_2H_2 ratios of 0.5, 1, 2 and 5 were 0.179, 0481, 0.493 and 0.864, respectively. Such an increase of CN concentration in the plasma discharge for higher N_2/C_2H_2 ratios can be explained by the greater energy available per unit mass of acetylene. This energy enhances the fragmentation probability of carbon triple bonds of the acetylene molecule and provides greater opportunity for abstraction of hydrogen from the structure. These interactions result in the formation of CN radicals due to the generation of atomic carbons that can subsequently react with nitrogen.

3.2. Surface chemistry of IPP films

To investigate the influence of N_2/C_2H_2 ratio on the chemical composition and structure of the IPP films, we analysed the samples using ATR-FTIR, XPS, ToF-SIMS, and ERDA. Fig. 3a shows ATR-FTIR spectra obtained for the IPP films deposited on Ti substrates. The spectra show a number of distinct peaks at wave numbers in the ranges of 1200−1500 cm^{-1}, 1500-1800 cm^{-1}, and 2100-2250 cm^{-1}. The peak at 1200−1500 is attributed to C−C and C−O, while the broad peak observed at 1500−1800 cm^{-1} is assigned to C=C, C=O, C≡N or N−H vibration modes [42,43]. The broad peak at 1500−1800 cm^{-1} widened with increases in the N_2/C_2H_2 flow ratio. These changes can be explained by the replacement of hydrogen with nitrogen atoms for the films deposited at relatively high N_2/C_2H_2 ratios. This explanation is in good agreement with the changes in the concentration of hydrogen atoms, as indicated by the ERDA results discussed later in this section. The peak recorded at 2100−2250 cm^{-1} is assigned to C≡N stretch in aliphatic and or aromatic nitriles [44,45]. This peak has also been previously assigned to nitrile and iso nitrile (−N≡C) groups bonded to hydrocarbon groups and aromatic rings [45,46]. The intensity of this peak increased by increasing the N_2/C_2H_2 ratio, an observation that is consistent with the OES results (Fig. 2) that showed greater concentrations of CN radicals are formed in the plasma phase for higher N_2/C_2H_2 ratios.

The elemental compositions of the IPP films were determined from XPS survey spectra and the results are plotted in Fig. 3b. Although the precursor gas mixture contained no oxygen, approximately 6% oxygen was detected for all the IPP films. The incorporation of oxygen is primarily due to the reaction of reactive
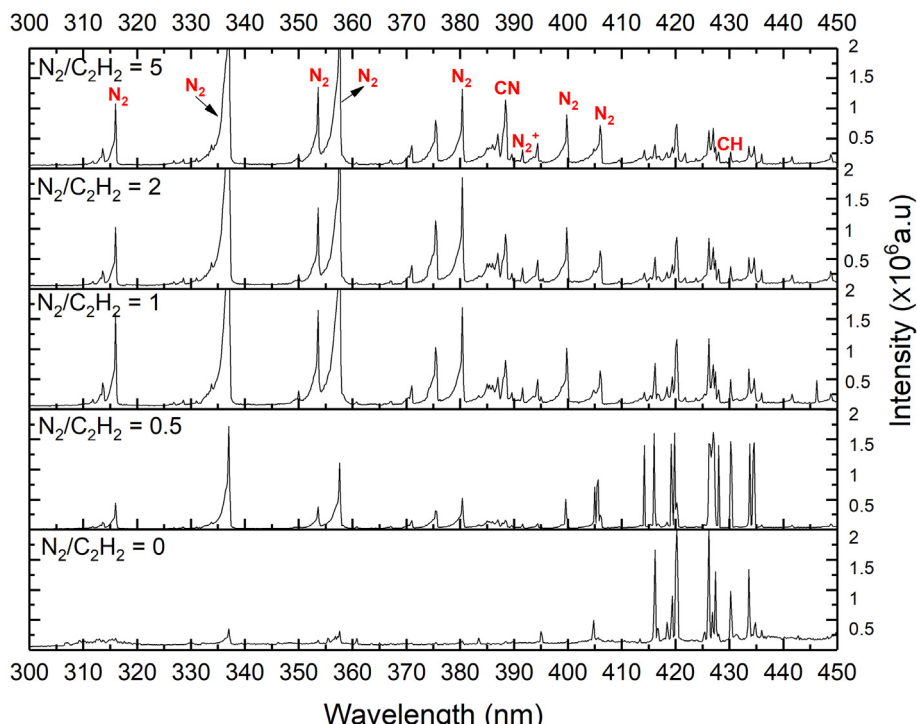
Fig. 2. Representative optical emission spectra in the wavelength range of 300–450 nm obtained from the plasma discharges during the deposition of IPP films with various N_2/C_2H_2 ratios present in the precursor gas mixture.

radials with atmospheric oxygen. This inevitable process is referred to as autoxidation and has also been observed before for other precursor monomers such as octadiene [47], thiophene [48], and trichloroethane [49]. By increasing the N_2/C_2H_2 flow ratio from 0 to 5, the nitrogen atomic concentration increased from 0% to 29.4%, while that of carbon decreased from 91.6% to 64.3%. The oxygen atomic concentration remained approximately unchanged at around 6%.

To gain further knowledge on bonding states of carbon and nitrogen in the IPP structure and to shed light on their sp^2/sp^3 hybridization character, we peak fitted the C1s XPS high resolution spectra, as shown in Fig. 3c. The C1s spectra were peak fitted by five components at binding energies 284.2 eV, 285.2 eV, 286 eV, 287.5 eV and 289.0 eV associated with C–C (sp^2), C–C (sp^3), C–N (sp^2)/C–O, C–N (sp^3)/C=O, and COOH, respectively [32,50–54]. For greater N_2/C_2H_2 ratios, the C1s peak becomes broader and more asymmetric due to the formation of higher concentrations of nitrogen-containing species. When increasing the N_2/C_2H_2 ratio from 0 to 5, for example, the FWHM increased from 1.952 ± 0.014 to 3.147 ± 0.025. These changes are in agreement with XPS survey spectra that showed higher atomic concentrations of nitrogen for the IPP films deposited using higher N_2/CH_2 ratios.

The sp^3 to sp^2 bonding ratio in carbon-containing organic films is one of the key parameters that regulates their mechanical properties and stability in aqueous environments. The total sp^3-hybridized carbon atoms in the IPP structure consist of sp^3-hybridized C–C bonds [C–C (sp^3)] and sp^3-coordinated C atoms bonded to N atoms [C–N (sp^3)]. The total sp^2-hybridized carbon atoms include those bonded to C atoms with sp^2 hybridization (C–C (sp^2)) as well as sp^2-coordinated C atoms bonded to N atoms (C–N (sp^2)). The variations of total sp^2 and sp^3 –bonded carbon

atoms as a function of the N_2/C_2H_2 ratio, estimated from the C1s high resolution spectra (Fig. 3c), are shown in Fig. 3d. Increases in the surface nitrogen atomic concentration resulted in the decrease of sp^3 and increase of sp^2 contents. With increasing nitrogen atomic concentration in the IPP film from 0% to 29.4%, the total sp^3 content reduced from 45.7% to 33.5%, whereas the total sp^2 bonded content increased from 45.6% to 63%. Such variations in the ratio of sp^2/sp^3 bonds agree with previous works where nitrogen was incorporated in amorphous carbon films deposited by ion beam assisted filtered arc deposition [55,56] or laser-induced pulsed arc [33].

The changes observed in the sp^3/sp^2 content of the IPP films from the C 1s high resolution spectra are further supported by those obtained from the N1s spectra, shown in Fig. 3c. Three components at BEs $\cong$ 398.8, 400.3, and 401.3 eV are fitted in the N1s spectra corresponding to N–C (sp^3), N–C (sp^2), and N–O, respectively [32,50–54]. The N–C (sp^3) bonding corresponds to threefold coordinated nitrogen atoms bonded to sp^3 carbon, and N–C (sp^2) is related to the substitution of N in graphite-like configurations and bonded to sp^2-coordinated C atoms [33,57]. Consistent with the trends observed in Fig. 3b, with the increase of nitrogen atomic concentration in the IPP films, the area percentage of N–C (sp^3) component decreased progressively, whilst that of N–C (sp^2) increased. The variations in the percentage of N–C (sp^3) and N–C (sp^2) are in agreement with previous works where nitrogen was incorporated in amorphous carbon films deposited by arc ion plating [58] or mass selected ion-beam deposition [57].

The variations observed in XPS surface chemistry correlate well with those observed in ToF-SIMS normalized positive counts and associated ion distribution maps. As shown in Fig. 4, increasing the N_2/C_2H_2 from 0 to 2 yielded a significant decrease in hydrocarbon counts, (CH_3, C_2H_3, and C_2H_5) and an increase in nitrogen-
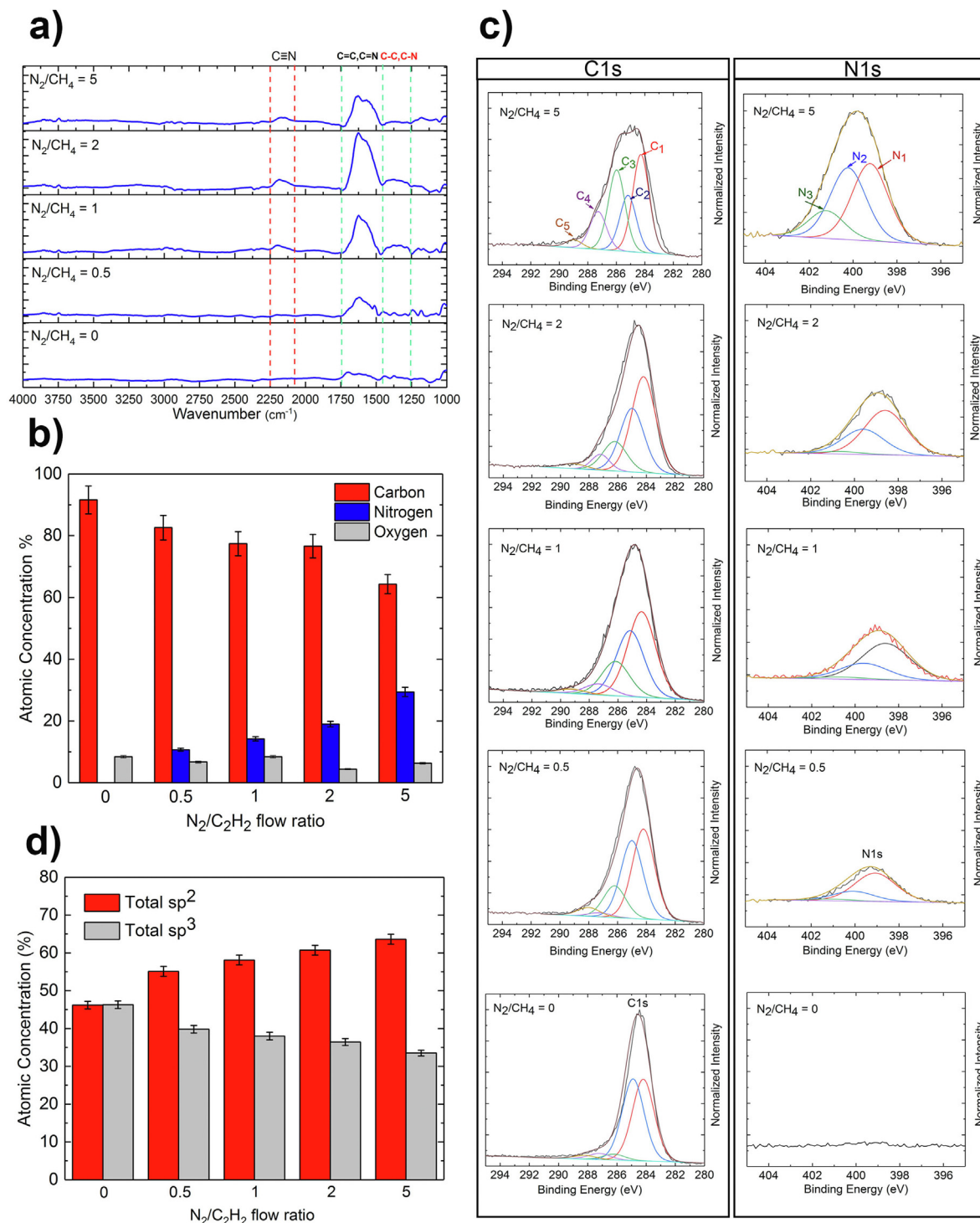
Fig. 3. FTIR and XPS surface chemistry analyses of IPP-coated Ti surfaces prepared using various N_2/C_2H_2 flow rate ratios. (a) FTIR spectra obtained in the range of 1000−4000 cm^{-1}. (b) XPS survey elemental composition of IPP-coated surfaces. (c) Normalized XPS C1s and N1s high-resolution spectra with C 1s fitted by five components: C_1: C−C (sp^2), C_2: C−C (sp^3), C_3: C−N (sp^2)/C−O, C_4: C−N (sp^3)/C═O, and C_5: COOH and XPS N 1s high-resolution spectra fitted by three components: N_1: N−C (sp^3), N_2: N−C (sp^2), and N3: N−O. (d) Total area percentage of the peaks fitted in the C1 high resolution spectra corresponding to sp^2 (C1 + C3) and sp^3 (C2 + C4) hybridized carbon atoms.

containing fragments (NH_4, CH_4N and C_2H_6N). These changes in the surface chemistry of IPP films agree with the OES data (Fig. 2) that showed higher concentrations of reactive nitrogen-containing

species, such as CN, are formed in the plasma phase for greater N_2/C_2H_2 flow rate ratios used in the precursor gas mixture.

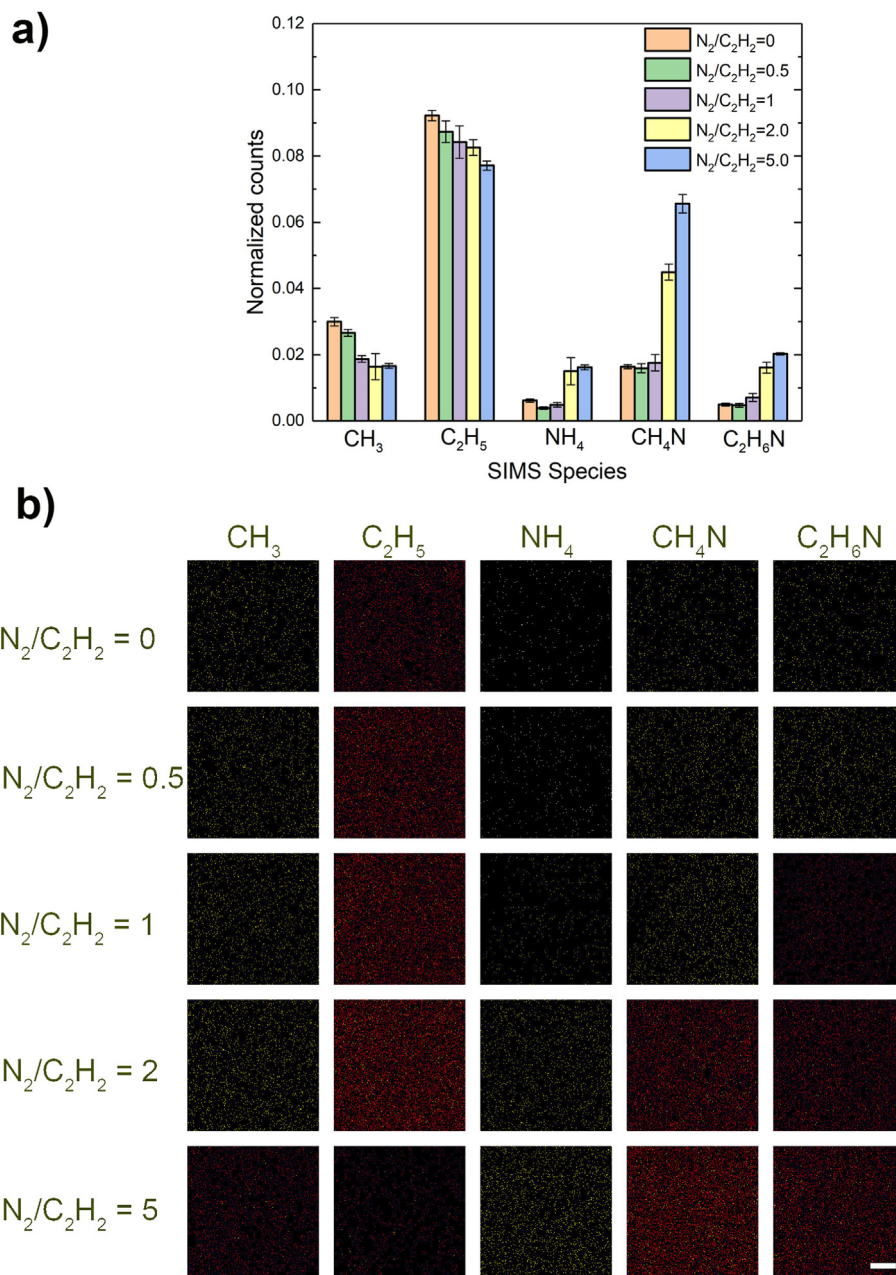Information on the hydrogen content of the IPP films provides

Fig. 4. (a) Normalized positive counts of ToF–SIMS species for IPP films deposited using various N_2/C_2H_2 flow rate ratios. (b) Representative ToF–SIMS positive ion distribution maps obtained for the IPP films. Scale bar = 20 μm.

useful insights into the mechanisms of polymerization with important implications for their physico-chemical stability for implant applications. However, hydrogen is not detectable by XPS as it doesn't contain core electrons. To measure the hydrogen content of the IPP films, we used elastic recoil detection analysis (ERDA). The ERDA hydrogen yield profiles of the films deposited with N_2/C_2H_2 flow ratios of 0, 2, and 5 (film thickness ≅ 180 nm) are plotted in Fig. 5. For all the profiles, hydrogen was absent at depths larger than approximately 200 nm, indicating that hydrogen originates mainly from the depths corresponding to the IPP film

thickness. The mean hydrogen yield values averaged within the depths of 50−150 nm were 90.5, 61.9, and 51.9 Cts/3 μC for the IPP films containing 0, 20 and 30 at% nitrogen, respectively. These results indicate that by increasing the N_2/C_2H_2 ratio in the precursor gas mixture, the concentration of hydrogen present in the film structure decreases. These changes can be primarily attributed to the lower availability of hydrogen atoms from the acetylene molecule for greater N_2/C_2H_2 ratios. In addition, for higher N_2/C_2H_2 ratios, more collisions between nitrogen and acetylene molecules occur per unit mass of acetylene, yielding a greater degree of
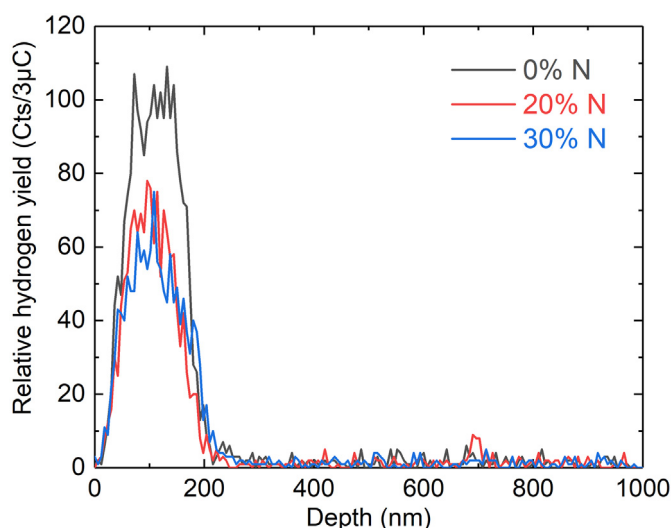
Fig. 5. The relative ERDA hydrogen yield profiles for IPP films containing various concentrations of nitrogen. The nitrogen atomic concentrations obtained from XPS results are indicated.

fragmentation. It is, therefore, plausible to suggest that under these conditions, a greater portion of hydrogen radicals are abstracted from C_2H_2 which can recombine and be evacuated from the plasma chamber in the form of H_2 [59–61]. Further, the abstraction of hydrogen from the IPP structure can also be facilitated by the presence of high concentrations of nitrogen in the gas mixture. We have recently shown that hydrogen atoms are extensively cleaved from the IPP polymer structures under the enhanced ion bombardment conditions of ion-assisted plasma polymerization [19]. In a nitrogen-rich reactive environment, such cleaved hydrogen atoms can be readily substituted by nitrogen, leaving behind IPP structures with lower hydrogen concentrations. This mechanism is consistent with the OES data that indicated the increase of CN concentration in the plasma discharge as a function of N_2/C_2H_2 ratio (Fig. 2), as well as with increases in the N-containing groups as confirmed by FTIR, XPS and ToF-SIMS results (Figs. 3 and 4).

3.3. Surface free energy of IPP films

The surface free energy (SFE) of biomaterials is of prime importance as it determines their wettability and how they interact with aqueous biological environments and the proteins within. The physico-chemical stability of polymeric films, e.g. their degree of swelling, adhesion and possible dissolution in liquid media is also greatly influenced by their SFE [62,63]. To calculate SFEs using liquid drop contact angles, the most reliable results can be obtained by applying a pair of liquids which have the largest polarity difference [64]. Thus, diiodomethane, as a non-polar liquid, and water, as a polar liquid, were used to measure contact angles and calculate the SFE and its polar and dispersive components for the IPP films polymerized using various N_2/C_2H_2 flow ratios.

As observed in Fig. 6a, by increasing the ratio of N_2/C_2H_2, the water contact angle decreased while that of diiodomethane increased. The SFE of the IPP films and their polar and dispersive components calculated using water and diiodomethane contact angles are plotted in Fig. 6b. By increasing the N_2/C_2H_2 ratio from 0 to 5, the total SFE increased from 53.3 mJ. m^{-2} to 70.07 mJ. m^{-2} and the polar component increased from 3.46 mJ. m^{-2} to 23.82 mJ. m^{-2}. No significant differences were observed for dispersive components as a function of N_2/C_2H_2. These results indicate that by increasing the nitrogen concentration in the precursor gas mixture, the hydrophilicity of the IPP film increases. Such increase in the hydrophilicity is due to the reduction in the concentration of non-polar hydrocarbon groups on the surface with the deposition of more polar nitrogen-containing groups as indicated by the XPS (Fig. 3b), FTIR (Fig. 3a), and ToF-SIMS (Fig. 4) results. We have previously shown that nano-thin plasma polymerized coatings, with thicknesses similar to the IPP coatings deposited in this work (<50 nm), follow the topography of the substrate with no significant influence on surface RMS roughness [17,47].

3.4. Refractive indices and cross-linking degrees of IPP films

We used spectroscopic ellipsometry to evaluate the changes in the refractive index (n) values of the IPP films as a function of their nitrogen atomic concentration, and the results are listed in Table 2. The cross-linking degree and the density of the films are correlated with their refractive indices [65–67]. The greatest refractive index
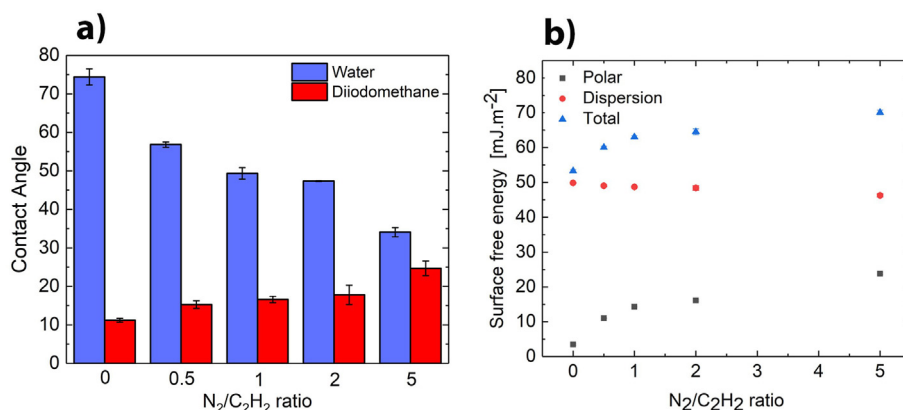

Fig. 6. Wettability of IPP films. a) static contact angles for water and diiodomethane drops placed on the IPP films deposited using various N_2/C_2H_2 flow rate ratios. b) The total surface free energy and corresponding dispersive and polar components for the IPP films as a function of N_2/C_2H_2 ratio. The results indicate that by increasing the nitrogen concentration in the precursor gas mixture, the hydrophilicity of the IPP film increases.

Table 2
Refractive index (n) values obtained from spectroscopic ellipsometry measurements for IPP films deposited using various N_2/C_2H_2 ratios measured at the wavelength of 630 nm.

N_2/C_2H_2 Flow rate ratio	Incorporated nitrogen (atomic %)	Refractive index (n) at 630 nm
0	0 ± 0.6	1.72 ± 0.002
0.5	10.7 ± 0.5	1.68 ± 0.001
1	14.2 ± 0.7	1.67 ± 0.003
2	19 ± 0.9	1.68 ± 0.003
5	29.4 ± 1.5	1.48 ± 0.001

(n = 1.72 ± 0.002), indicative of the highest degree of cross-linking and densification, was measured for the IPP film containing no nitrogen. In contrast, the film with the maximum concentration of nitrogen (29.4%) showed the lowest degree of cross linking and densification, as indicated by its lowest n value (1.48 ± 0.001). These results are in alignment with the trends reported in previous works on PECVD films. For example, Ficek et al. showed that the refractive index of diamond-like thin films, deposited using microwave PACVD of $CH_4/H_2/N_2$, decreased from approximately 2.6 to 2.4 as a result of increasing the nitrogen content from 1 to 8% [68]. Another example of a similar trend is reported by Gharibian and co-workers who demonstrated that the refractive index of diamond-like films deposited from mixtures of toluene and nitrogen decrease as a function of nitrogen concentration for plasma powers in the range of 50−90 W [69]. The reduction in the values of n for IPP films containing higher nitrogen atomic concentrations can be attributed to increases in the ratio of sp^2 to sp^3 hybridised carbon atoms (Fig. 3d) which in turn reduces the IPP films' degree of cross-linking and density. Such variations in the cross-linking degree of the IPP films have important implications for understanding the mechanisms underpinning their nanomechanical properties and physico-chemical stability as discussed in the next sections.

3.5. Nano-mechanical properties of IPP films

To quantitively evaluate the role of nitrogen on the stiffness, residual stress and scratch resistance of the IPP films, we preformed nano-indentation, stylus profilometry, and nano-scratch tests, respectively. Fig. 7a compares the variations of elastic modulus as a function of indentation depth for the uncoated titanium substrate and those coated with IPP films containing 0% ($N_2/C_2H_2 = 0$) and 20% ($N_2/C_2H_2 = 2$) nitrogen. The elasticity modulus for the bare Ti substrate was ~168 GPa for an indentation depth of 14.0 ± 1.7 nm, and it reduced to about 125 GPa for indentation depths larger than 60 nm. Such decreasing trend of the measured elasticity as a function of indentation depth can be attributed to the presence of a native oxide layer with a thickness of up to 10 nm on the Ti surface [70]. The elastic modulus for the IPP-coated Ti surfaces, however, rose as the indentation penetrated deeper up to 150 nm and remained constant at approximately 120 GPa as the indentation progressed further into the substrate. Particularly important is the changes of the elastic modulus for shallow indentation depths, where the substrate's influence is minimum. For the shallow depths (displacement <100 nm), significantly lower Young's moduli were measured for the film with 20% nitrogen compared to the one with 0% N. For example, the elastic modulus at an indentation depth of 25 nm was 85 GPa and 42 GPa for the 0% and 20%N IPP films, respectively.

To evaluate the residual stress of the films, we used stylus profilometry to calculate the silicon wafers' radii of curvature before and after IPP deposition. The profiles of the IPP-coated silicon wafers with 0% and 20% N are shown in Fig. 7b. The residual stress values calculated using these profiles were 0.57 and 0.20 GPa for the films containing 0 and 20% N, respectively. The higher compressive residual stress of the IPP film with no nitrogen is due to its denser structure as indicated by both its higher content of sp^3 hybridization compared to the film with 20% N and its greater refractive index value (Table 2). The highly cross-linked structure of the IPP film with no nitrogen plays a key role in restricting mobility and hindering stress relief during the film growth [71].

To gain further knowledge on the mechanical performance of the IPP films modulated by the incorporation of nitrogen, we preformed ramp load nano-scratch tests over a length of 200 μm. In these tests, the 'critical load' (CL) refers to the lateral force at which the film delaminates from the Ti substrate [72,73]. The representative scratch test results showing the variations of normal and lateral forces as a function of scratch distance together with associated post-scratch optical microscopy images are presented in Fig. 7c. As observed from the post-scratch optical profiles, the delamination of the 0%N film took place within the first few micrometres of the scratch line (CL = 0.5 mN), whereas the failure of the 20%N film occurred at a scratch length of approximately 140 μm (CL = 37 mN). The significantly greater critical load achieved for the nitrogen-containing film correlates well with the enhanced elasticity (Fig. 7a) and reduced internal stress (Fig. 7b) measured for this sample.

The role of nitrogen in enhancing the elasticity and resistance to plastic deformation of the IPP films can be explained by taking the surface chemistry results into account. These results showed a greater ratio of sp^2/sp^3 hybridized bonds for the films containing higher concentrations of nitrogen (Fig. 3d). The length of sp^2 C=N bonds is shorter than that for either sp^2 C=C or sp^3 C−C bonds [36]. Therefore, the incorporation of nitrogen into the IPP film atomic structure endows a more elastic structure and consequently greater resistance to cohesive deformation [36,74]. Further, the replacement of carbon by nitrogen in the IPP structure results in the reduction of average coordination number and overstraining because nitrogen atoms can admit a coordination number of maximum 3 compared to carbon atoms that can have a maximum coordination number of 4. Another possible explanation for the superior elasticity of the nitrogen-containing film is the formation of C≡N groups, as revealed by FTIR results (Fig. 3a), which decrease the connection between carbon networks and interlinks the sp^2 clusters, yielding a lower density, polymeric-like structure with lower compressive stress [32,74]. This explanation agrees well with the works on tetrahedral amorphous carbon films reporting that the incorporation of nitrogen into these films leads to decreases of residual stress in the films due to the reduction of average coordination number by transformation of sp^3 to sp^2 carbon bonds and the formation of C≡N groups [32,74].
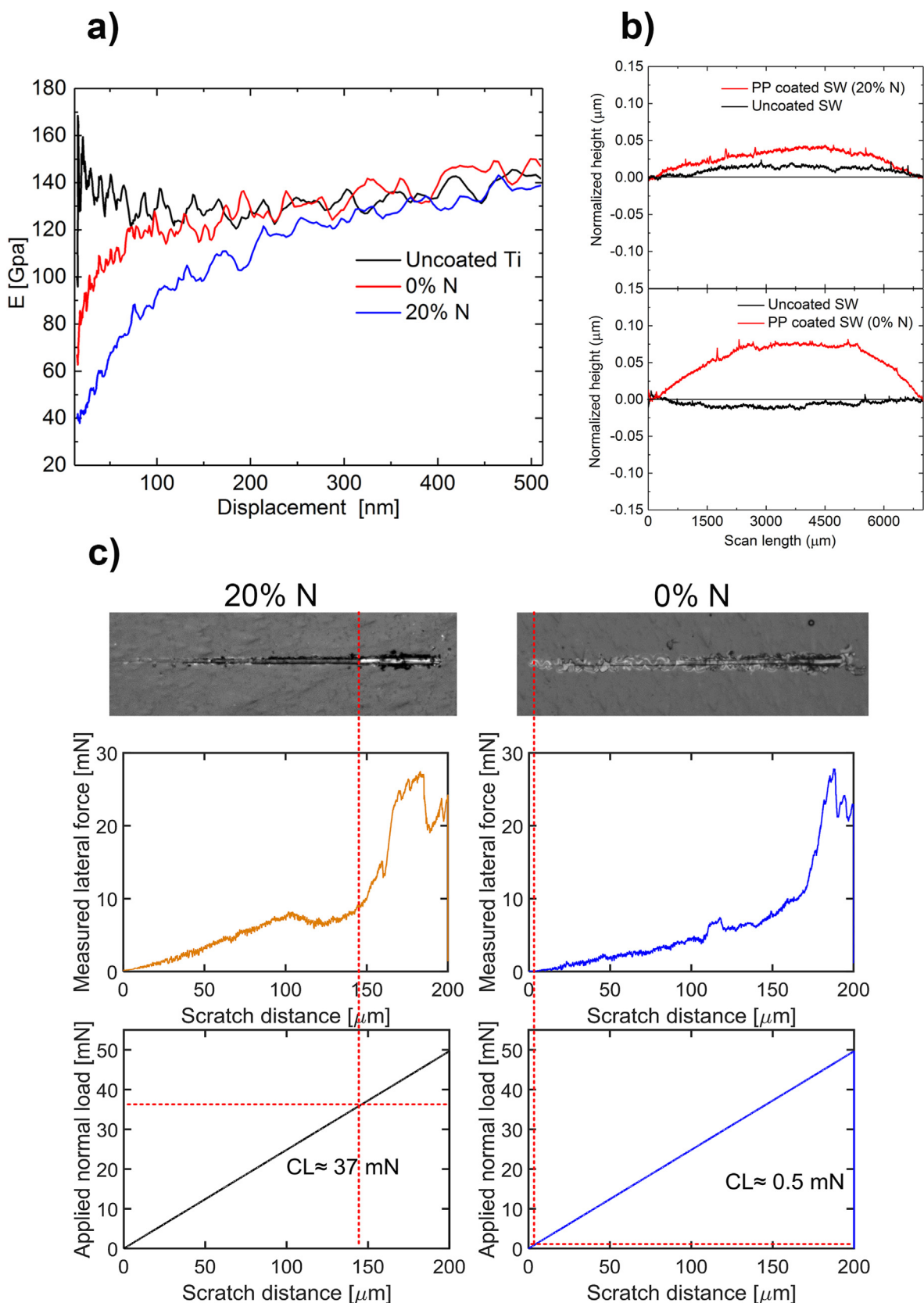
Fig. 7. Nano mechanical characterization of IPP films with nitrogen atomic concentrations of 0 and 20%. a) The elastic modulus as a function of indentation depth obtained for uncoated and IPP-coated Ti samples. b) Profiles of uncoated and IPP-coated silicon wafer substrates. c) Nano scratch test results with critical loads (CL) indicated and the associated post-scratch optical images obtained for the IPP-coated titanium samples. The normal loads at which the IPP films delaminated from the titanium surfaces are identified as CL. The vertical dash line is associated with the first discontinuity occurring in the lateral force-distance curve, and the first delamination point observed in post-scratch images. At this scratch distance, the normal load (CL) was recorded as indicated by the horizontal dash line.
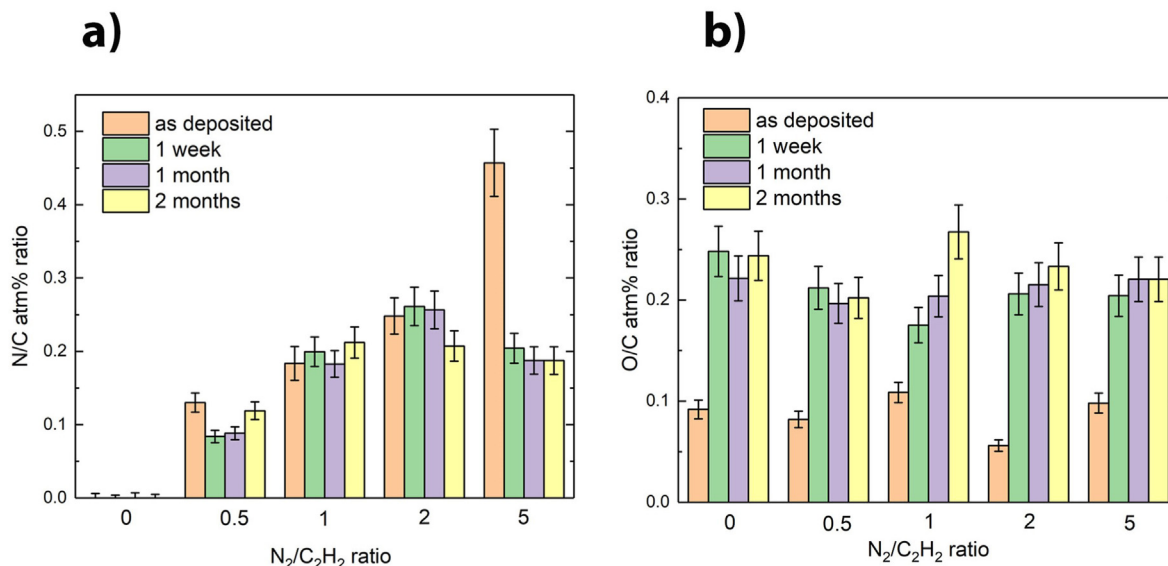
Fig. 8. a) N/C and **b)** O/C atomic percent ratios obtained from XPS measurements for the IPP films deposited using various N_2/C_2H_2 flow rate ratios before and after incubation in Tyrode's SBF solution for the durations of 1 week, 1 month and 2 months.

3.6. Physico-chemical stability of IPP films in simulated body fluid (SBF)

Mechanical robustness and physico-chemical stability of coatings are vital for surface modification of biomedical devices, in particular for bone implants that undergo elastic and plastic deformation during surgical insertion. Nitrogen-rich plasma polymer films are, however, susceptible to loss of nitrogen-containing moieties in aqueous media [75]. The loss of nitrogen accompanied by extensive oxidation of a plasma polymer film not only alters the surface chemistry but may also result in loss of integrity or severe degradation of the films in a short time frame [76]. To evaluate the chemical and physical stability of the IPP films in biologically-relevant environments, we incubated the samples in Tyrode's simulated body fluid (SBF) at 37 °C for durations of up to 2 months.

Fig. 8a shows the XPS N/C atomic concentration ratios of the IPP films, deposited using various N_2/C_2H_2 flow rate ratios, before and after incubation in the SBF solution. The changes in N/C ratio were minimal for the IPP films with N_2/C_2H_2 ratio less than 5, even after 2 months incubation in the SBF solution. In contrast, there was a substantial decrease in N/C ratio for the sample deposited using the N_2/C_2H_2 ratio of 5 after 1 week of incubation in SBF. Such a sharp decrease in N/C ratio can be described by extensive out-diffusion of nitrogen-containing species, such as NH_3, that could have been locked in the IPP structure during the polymerization process. Also, the hydrophilic character of this sample (WCA of 74.4°) encourages the penetration of water molecules into the film structure as well as the out-diffusion of polar nitrogen-containing compounds into the SBF solution. This diffusion-based mechanism is further validated by the refractive index results (Table 2), showing that the IPP film containing the highest concentration of nitrogen has the lowest degree of crosslinking among all the films. A loosely cross-linked structure provides higher mobility and a more open structure to facilitate the ingress of O_2 and H_2O molecules into the film with easy access to reactive sites, as well as facilitating out-diffusion of

low molecular weight species [77,78]. The degradation rate of polymeric films in aqueous environments is directly correlated with the ingress rate of dissolved oxygen and water molecules into the film structure [79]. The O/C ratio increased significantly for all samples after 1 week of incubation in SBF solution (Fig. 8b). This increase of O/C is due to the oxidation of the carbon-centered radicals into more stable species at the surface of the films. The oxidation process is also accelerated by hydrogen abstraction from the nitrogen-containing groups [75].

Physical stability and adhesion of a polymeric film to the substrate is of crucial importance particularly for mechanically demanding applications such as bone implants. To evaluate the mechanical adhesion of the IPP films to the titanium substrate, we carried out a tape test after cutting an 'X' through the films (ASTMD 3359−09). The SEM images of the films with nitrogen atomic concentrations of 0% and 20% before and after the tape test are shown in Fig. 9. Following the tape test, significant portions of the film that contained no nitrogen were peeled off from the substrate, whilst no signs of peeling or delamination were observed for the film with 20% N.

Bone implants are likely to be scratched during insertion into the body. It is therefore essential that the film resists delamination from the substrate in the harsh body environment even when scratched. To simulate this scenario, we scratched the IPP films before their incubation in the SBF solution at 37C for two months and evaluated their physical robustness using SEM images, shown in Fig. 9. Consistent with the tape test results, failure in the form of buckling formation or delamination was evident for the 0% N film near the scratch site and the sample edge, whereas no evidence of failure was observed for the film with 20% N.

The superior mechanical stability for the IPP film achieved by the incorporation of nitrogen in the structure is well explained by its lower stiffness and smaller compressive residual stress as indicated by the profilometry and nano-indentation data (Fig. 7). A film with residual compressive stress buckles out of its substrate plane once the compressive force surpasses a critical threshold [80].
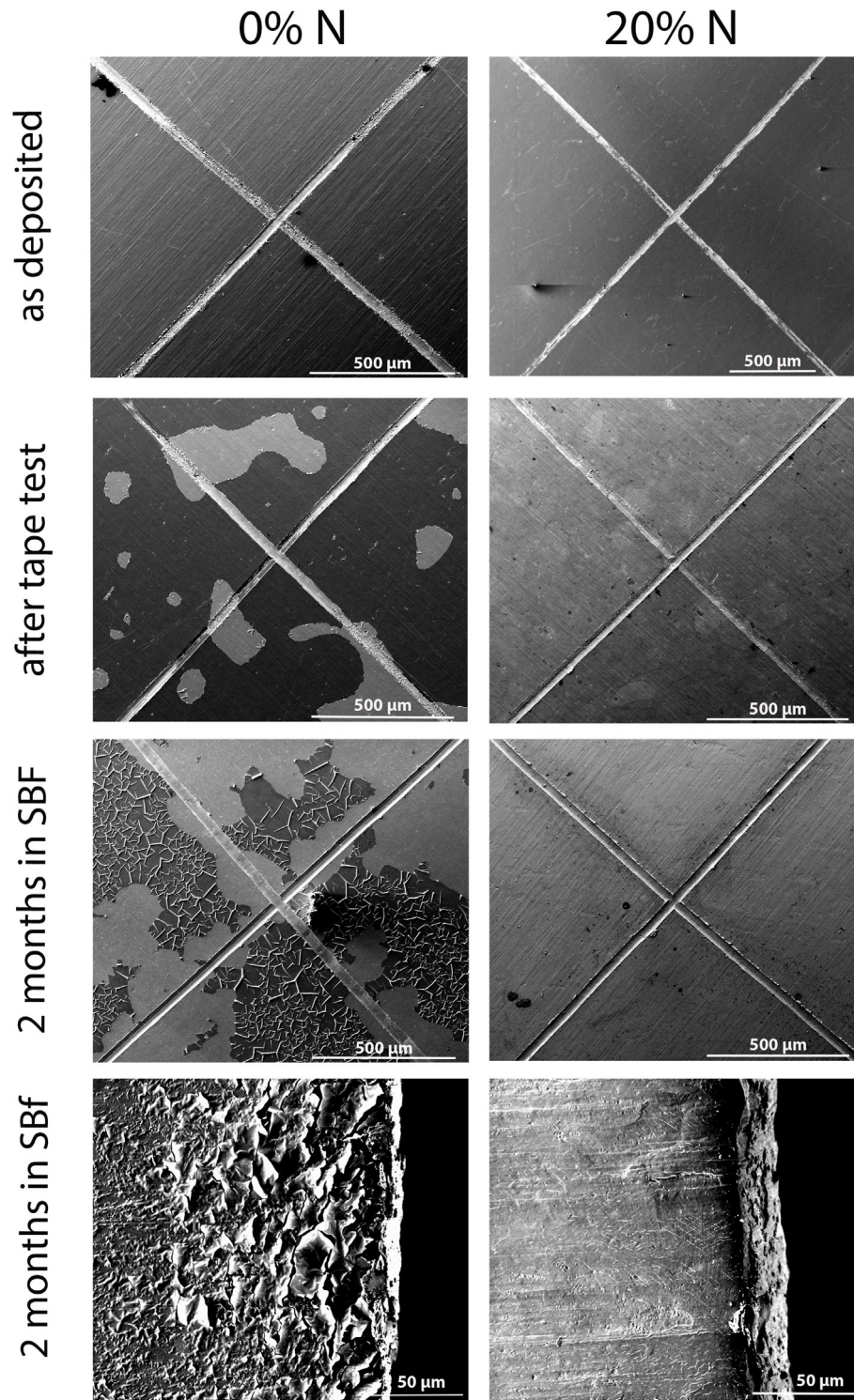
Fig. 9. SEM images of IPP films deposited on titanium surfaces with 0% and 20% N before and after the tape adhesion test and incubation in SBF at 37 °C for two months. The samples were scratched before the adhesion tape test and incubation in SBF to mimic a scenario where the IPP film is physically damaged during surgical insertion.

Hence, polymeric films that are either poorly attached to the substrate with weak interfaces or have high degrees of residual compressive stress are prone to failure by forming buckles and/or delamination. In our previous study, we demonstrated that the formation of metallic carbide bonds at the early stages of the IPP film deposition under enhanced ion bombardment enables the formation of strong IPP film-substrate interfaces [26]. The results presented here show that incorporating nitrogen into the IPP film's
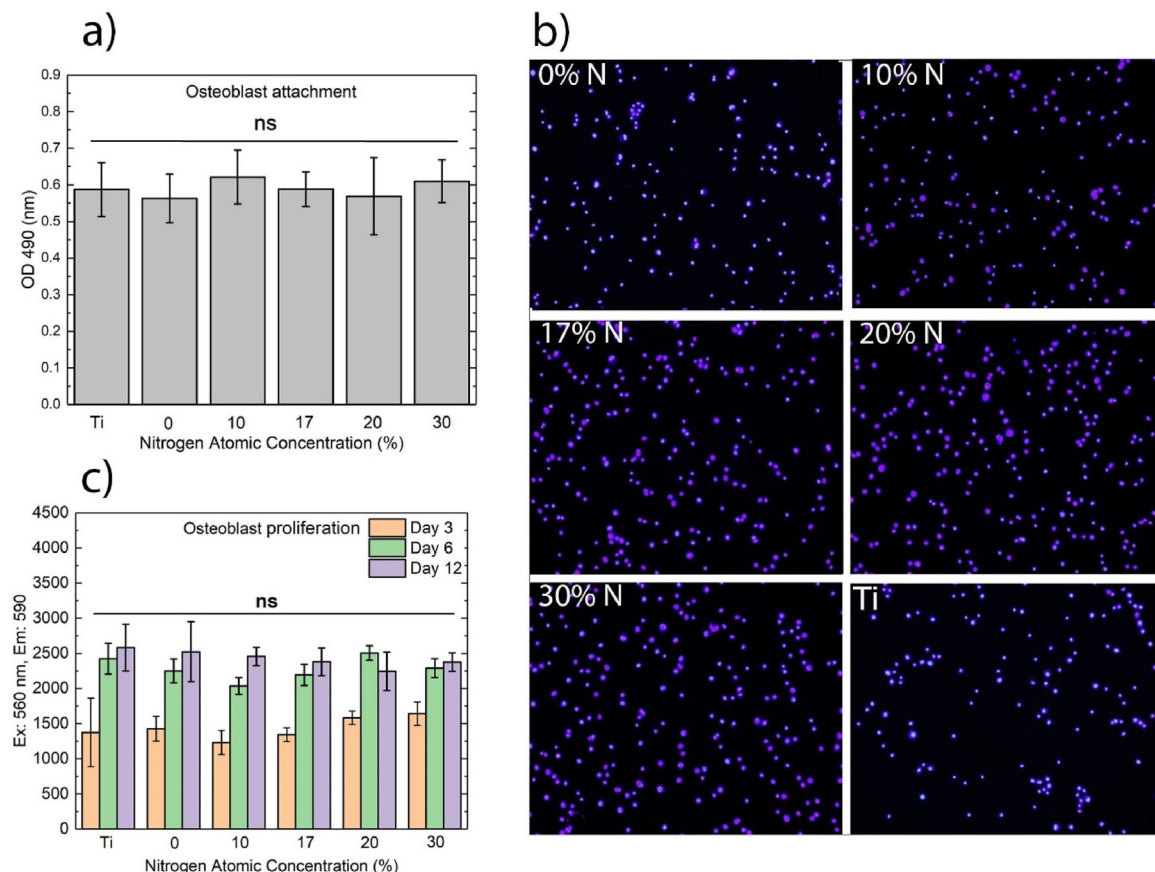
Fig. 10. Primary osteoblast cellular absorbance on the IPP films containing various nitrogen atomic concentrations. **(a)** Primary mouse osteoblast attachment results and **(b)** representative images of osteoblast cells attached on IPP films. **(c)** Osteoblast proliferation results obtained for the same IPP-coated surfaces at 3, 6, 12, and 15 day time points.

structure reduces the residual compressive stress, thus dramatically reducing the probability of physical failure; a conclusion also supported by nano-scratch test results (Fig. 7c). These results together underpin the pivotal advantage of nitrogen incorporation into the IPP structure to achieve highly robust interfaces that withstand failure in biological related media.

3.7. Cellular responses and covalent biofunctionalization of IPP films

To evaluate cellular responses on the IPP films containing various concentrations of nitrogen, we seeded primary osteoblasts (OB) on the surfaces. No significant difference was observed in osteoblast attachment on the IPP films with different nitrogen contents as observed from Fig. 10a. Representative fluorescence images of OB cells attached to the surfaces also confirm these results (Fig. 10b). To further evaluate the biological effect of the nitrogen present in the films, we compared cell proliferation on the surfaces after 3, 6, and 12 days of culture. The results are shown in Fig. 10c, and in line with cell attachment data, they indicate that the films' nitrogen concentration has no significant effect on OB proliferation. Nitrogen-containing functional groups such as amides and amines, rather than the total nitrogen concentration, have previously been shown to promote cell attachment and proliferation [81–84]. For example, Griesser et al. coated the surfaces of fluorinated ethylene propylene copolymer (FEP) by plasma polymerization of volatile amine- and amide-containing monomers, and showed that such films improve the colonization of both human dermal fibroblasts and endothelial cells [84]. The general biocompatibility, similar to that of Ti, observed across all the IPP films is important and favourable. Equal cellular responses to all IPP films indicate that the nitrogen content can be used as a free parameter without cytotoxicity concerns to optimise the IPP films' physical durability and chemical stability. Therefore, based on the stability and robustness criteria and informed by the results presented in Section 3.6, we used the IPP film containing 20%N for covalent biofunctionalization experiments.

The IPP films deposited under enhanced ion bombardment, facilitated by a negative bias voltage applied to the titanium substrate [26], contain high concentrations of radicals embedded in subsurface layers. These radicals facilitate the covalent attachment of biomolecules that contact the surface. The electron spin resonance (ESR) spectrum of the optimized IPP film (20% N), shown in **Supplementary Information** (**Figure SI**), consisted of a single resonance peak at 3515 G, corresponding to a g-value of 2.003, and confirmed that the film was permeated with unpaired electrons, i.e. in radical groups with dangling bonds. To determine whether these radicals present in the IPP film structure can bestow single-step, covalent biomolecule functionalization of materials prior to their implantation in the body, we incubated uncoated and IPP-coated Ti surfaces in a buffer solution containing fibronectin (FN) as a model ECM biomolecule. Fibronectin contains the bioactive arginine-
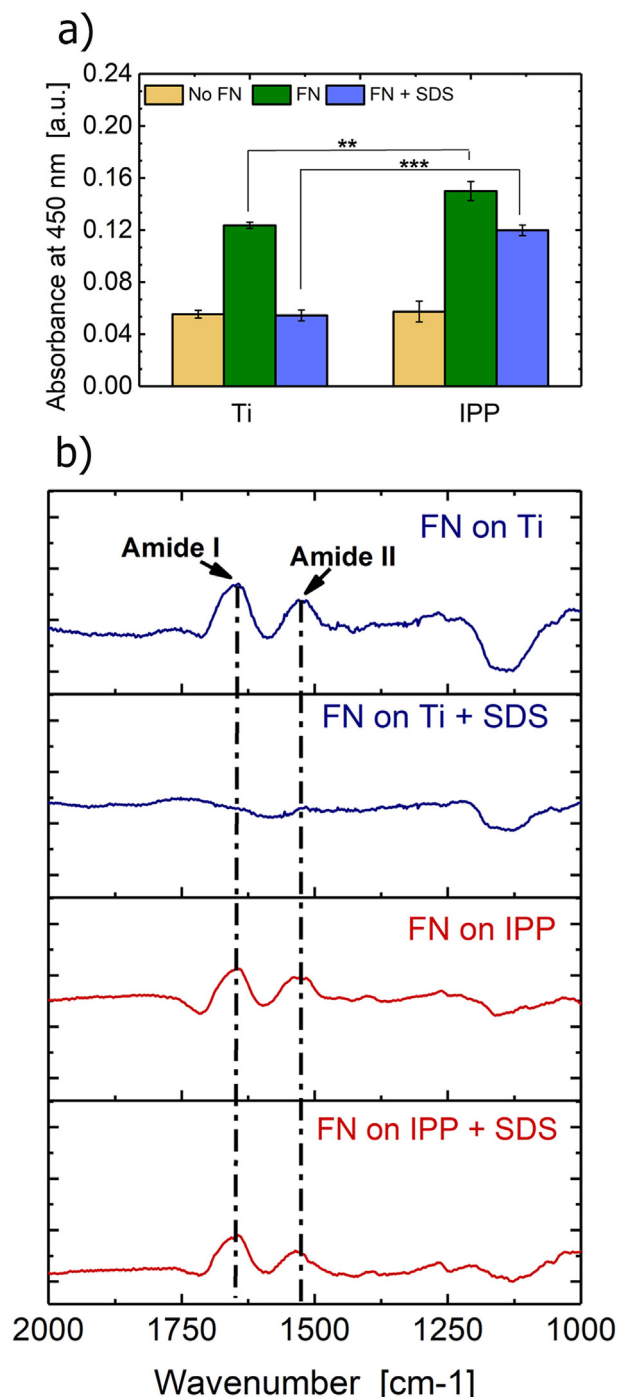
Fig. 11. (a) ELISA signals from surface-bound FN protein on the uncoated Ti and IPP-coated samples before and after SDS detergent washing. (b) ATR FT-IR spectra obtained for uncoated and IPP-coated Ti incubated in FN solution with and without SDS detergent washing.

glycine-aspartic acid (RGD) adhesive sequence which stimulates integrin mediated cell adhesion. With regard to orthopaedic implants, fibronectin can effectively enhance new bone formation through regulating the differentiation and survival of osteoblasts [85,86]. The fibronectin receptor α5β1 has been shown to promote osteoblastic differentiation [87,88]. To demonstrate the covalent

nature of biofunctionalization, stringent washing at an elevated temperature of 70 °C using sodium dodecyl sulfate (SDS) was employed. SDS is an ionic detergent that disturbs physical bonds at the surface, while leaving covalent bonds intact [89,90].

We used ELISA and ATR-FTIR spectroscopy to assess the presence of FN molecules on the surfaces before and after the SDS wash. The ELISA results for specimens incubated in fibronectin buffer are shown in Fig. 11a. The observed reduction in the amount of immobilized fibronectin on the IPP-coated surface after SDS wash was much smaller compared to the uncoated titanium. Almost 80% of the proteins remained on the IPP-coated surface; whereas the signal from the bare titanium surface was reduced to the background level observed on the control surface that had not been exposed to fibronectin. The resilience of fibronectin molecules against rigorous detergent washing is indicative of the ability of IPP films to covalently attach and retain biomolecules through reactions with surface-embedded radicals.

The ATR FT-IR spectra of fibronectin on the uncoated and IPP-coated Ti, before and after SDS washing, are shown in Fig. 11b. To reveal the peaks related to the protein molecules, the spectra of IPP-coated or uncoated titanium without fibronectin were subtracted from those with fibronectin. In the case of IPP-coated titanium, two peaks of Amide I ($1650 \, cm^{-1}$) and Amide II ($1540 \, cm^{-1}$), assigned to amide bonds that form the backbone of the fibronectin molecules, were observed for both before and after SDS washing conditions. In contrast, these peaks were not detected on the uncoated titanium after SDS washing, indicating that the physisorbed fibronectin molecules were removed by SDS washing. These results reinforce the ELISA observation, confirming that fibronectin is covalently attached to the IPP-coated titanium surface.

The primary osteoblast cell attachment on the fibronectin-IPP coated surface was compared to the IPP-coated and uncoated titanium samples, and the results are shown in Fig. 12a. The osteoblast cell number on the uncoated titanium was not significantly different from that on the IPP-coated sample. However, the cell population on the fibronectin-IPP coated surface was significantly higher than the other two surfaces, indicative of a biofunctional interface where covalently anchored fibronectin molecules retained their functionality, providing focal adhesion sites that mimic those of the native extra cellular matrix (ECM). Such biofunctionality is visually demonstrated by representative images showing a greater population of osteoblast cells attached to FN-functionalized IPP-coated Ti compared with a bare surface (Fig. 12b). These highly robust, nitrogen-rich IPP coatings, therefore, hold great promise as platforms to employ biomimicry for enhancing biofunctionality with pivotal implications in surface engineering of implants including bone implantable medical devices.

We have previously shown that the reactive radicals embedded in IPP coatings also enable covalent attachment of antimicrobial agents, such as MEL4 and caspofungin, exhibiting favourable *in vitro* antibacterial and antifungal activities [17]. Future studies will investigate co-immobilization of ECM and bone-signalling biomolecules as well as antimicrobial agents on the IPP-coated surfaces to create multifunctional interfaces that are both biomimetic and antimicrobial. Further, the sample holder used for ion-assisted plasma polymerization can be retrofitted into a conductive rotating cage that is negatively biased, while it is immersed in RF plasma of a polymerizable gas. This strategy can enable homogenous deposition of IPP coatings onto 3D substrates, such as dental implants and tissue engineering scaffolds, for future *in vivo* studies.
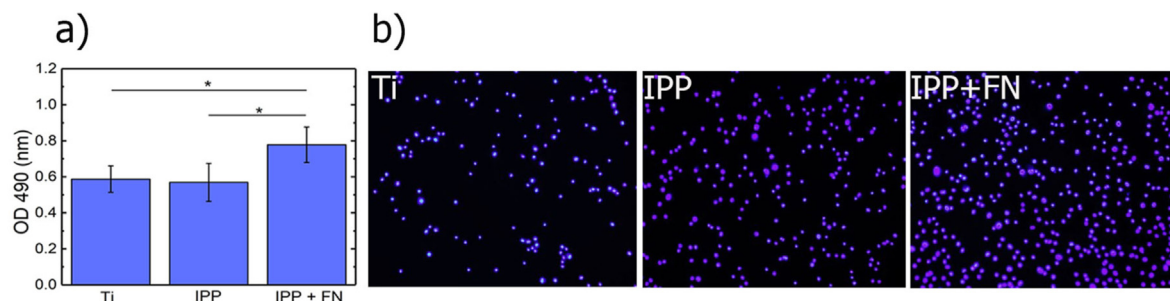
Fig. 12. (a) Primary osteoblast attachment on the bare Ti, IPP-coated Ti, and IPP-coated Ti + FN surfaces. (b) Representative images of osteoblast cells attached to the surfaces after 1 h.

4. Conclusions

To modulate the physico-chemical stability of ion-assisted plasma polymerized films, we pursued a simple approach of nitrogen incorporation in their structure (0−30 atomic%) by tuning the nitrogen (N_2) to acetylene (C_2H_2) flow rate ratio used in the precursor gas mixture. We provided evidence that the incorporation of nitrogen increases the ratio of sp^2/sp^3 bonded atoms, thus reducing the stiffness and residual compressive stress of the films. These microstructural changes had important implications for achieving a highly robust IPP film with 20% N that resisted any form of failure after incubation in Tyrode's simulated body fluid for 2 months, even when scratched or mechanically deformed. Across the range of nitrogen atomic concentrations, similar responses were observed in the attachment and proliferation of primary osteoblasts seeded on the surfaces, suggesting that the nitrogen content can be used as a free parameter without reduced biocompatibility or cytotoxicity concerns to optimise the films' physical durability and chemical stability. Cell assays showed that covalently-tethered fibronectin molecules were effective in significantly increasing the attachment and proliferation of primary osteoblast cells, suggesting that they retained their native-like conformations on the IPP coatings. The combination of chemical stability, mechanical durability, and enhanced osteoblast attachment and proliferation make the developed IPP coating a highly promising candidate for surface engineering of next-generation implantable medical devices such as bone implants.

Data availability

The authors declare that all data supporting the findings of this study are available within the article and its supplementary information files or from the corresponding author upon request.

Author statement

Omid Sharifahmadian: Investigation, Visualization, Writing − original draft; **Chongpu Zhai**: Investigation; **Juichien Hung**: Investigation; **Ghazal Shineh**: Data Formal analysis, Writing − review & editing; **Callum A.C. Stewart**: Investigation; **Arifah A. Fadzil**: Investigation; **Mihail Ionescu**: Investigation; **Yixiang Gan**: Investigation; **Steven G. Wise**: Investigation, Review & Editing, Supervision; **Behnam Akhavan**: Conceptualisation, Methodology, Investigation, Visualization, Writing − original draft, Writing − review & editing, Supervision, Funding acquisition

Declaration of competing interest

The authors declare that they have no known competing financial interests or personal relationships that could have appeared to influence the work reported in this paper.

Appendix A. Supplementary data

Supplementary data to this article can be found online at https://doi.org/10.1016/j.mtadv.2021.100188.

References

[1] N. Vaughan, V.N. Dubey, T.W. Wainwright, R.G. Middleton, A review of virtual reality based training simulators for orthopaedic surgery, Med. Eng. Phys. 38 (2) (2016) 59−71, https://doi.org/10.1016/j.medengphy.2015.11.021.
[2] B.A.J.A. Van Oirschot, et al., Osteophilic properties of bone implant surface modifications in a cassette model on a decorticated goat spinal transverse process, Acta Biomater. 37 (2016) 195−205, https://doi.org/10.1016/j.actbio.2016.03.037.
[3] C. Stewart, B. Akhavan, S.G. Wise, M.M.M. Bilek, A review of biomimetic surface functionalization for bone-integrating orthopedic implants: mechanisms, current approaches, and future directions, Prog. Mater. Sci. 106 (July) (2019) 100588, https://doi.org/10.1016/j.pmatsci.2019.100588.
[4] X. Shen, et al., Fabrication of magnesium/zinc-metal organic framework on titanium implants to inhibit bacterial infection and promote bone regeneration, Biomaterials 212 (April) (2019) 1−16, https://doi.org/10.1016/j.biomaterials.2019.05.008.
[5] G. Ciobanu, M. Harja, Cerium-doped hydroxyapatite/collagen coatings on titanium for bone implants, Ceram. Int. 45 (2) (2019) 2852−2857, https://doi.org/10.1016/j.ceramint.2018.07.290.
[6] Y. He, et al., Peptide LL-37 coating on micro-structured titanium implants to facilitate bone formation in vivo via mesenchymal stem cell recruitment, Acta Biomater. 80 (2018) 412−424, https://doi.org/10.1016/j.actbio.2018.09.036.
[7] J.H. Lee, et al., Non-thermal atmospheric pressure plasma functionalized dental implant for enhancement of bacterial resistance and osseointegration, Dent. Mater. 33 (3) (2017) 257−270, https://doi.org/10.1016/j.dental.2016.11.011.
[8] R. Smeets, et al., Impact of dental implant surface modifications on

osseointegration, BioMed Res. Int. 2016 (2016), https://doi.org/10.1155/2016/6285620.

[9] S.A. Alves, et al., Synthesis of calcium-phosphorous doped TiO 2 nanotubes by anodization and reverse polarization: a promising strategy for an efficient biofunctional implant surface, Appl. Surf. Sci. 399 (2017) 682−701, https://doi.org/10.1016/j.apsusc.2016.12.105.

[10] C. Ferreira, J. Babu, A. Hamlekhan, S. Patel, T. Shokuhfar, Efficiency of nanotube surface−treated dental implants loaded with doxycycline on growth reduction of porphyromonas gingivalis, Int. J. Oral Maxillofac. Implants 32 (2) (2017) 322−328, https://doi.org/10.11607/jomi.4975.

[11] B. Henriques, et al., Influence of laser structuring of PEEK, PEEK-GF30 and PEEK-CF30 surfaces on the shear bond strength to a resin cement, J. Mech. Behav. Biomed. Mater. 84 (May) (2018) 225−234, https://doi.org/10.1016/j.jmbbm.2018.05.008.

[12] J. Li, X. Cui, G.J. Hooper, K.S. Lim, T.B.F. Woodfield, Performance of hybrid additive manufactured titanium implants for orthopaedic applications : a review, J. Mech. Behav. Biomed. Mater. (2020) 103671, https://doi.org/10.1016/j.jmbbm.2020.103671.

[13] M. Badv, F. Bayat, J.I. Weitz, T.F. Didar, Jo Ur L P of, Elsevier, 2020.

[14] J. Pre-proof, Biofunctionalized chondrogenic shape-memory ternary scaffolds for efficient cell-free cartilage regeneration, Acta Biomater. (2020), https://doi.org/10.1016/j.actbio.2020.01.015.

[15] S.E. Kim, et al., Improving osteoblast functions and bone formation upon BMP-2 immobilization on titanium modified with heparin, Carbohydr. Polym. 114 (2014) 123−132.

[16] H.-Y. Ao, et al., Covalently immobilised type I collagen facilitates osteo-conduction and osseointegration of titanium coated implants, J. Orthop. Transl. 5 (2016) 16−25.

[17] B. Akhavan, et al., Plasma activated coatings with dual action against fungi and bacteria, Appl. Mater. Today 12 (2018) 72−84, https://doi.org/10.1016/j.apmt.2018.04.003.

[18] B. Akhavan, et al., Direct covalent attachment of silver nanoparticles on radical-rich plasma polymer films for antibacterial applications, J. Mater. Chem. B (2018), https://doi.org/10.1039/c8tb01363b.

[19] B. Akhavan, et al., Radical-functionalized plasma polymers: stable biomimetic interfaces for bone implant applications, Appl. Mater. Today 16 (2019) 456−473, https://doi.org/10.1016/j.apmt.2019.07.002.

[20] C.A.C. Stewart, et al., Multifunctional protein-immobilized plasma polymer films for orthopedic applications, ACS Biomater. Sci. Eng. 4 (12) (2018) 4084−4094.

[21] M.M.M. Bilek, et al., Free radical functionalization of surfaces to prevent adverse responses to biomedical devices, Proc. Natl. Acad. Sci. Unit. States Am. 108 (35) (2011) 14405−14410.

[22] M. Santos, E.C. Filipe, P.L. Michael, J. Hung, S.G. Wise, M.M.M. Bilek, Mechanically robust plasma-activated interfaces optimized for vascular stent applications, ACS Appl. Mater. Interfaces 8 (15) (2016) 9635−9650.

[23] L.J. Martin, B. Akhavan, M.M.M. Bilek, Electric fields control the orientation of peptides irreversibly immobilized on radical-functionalized surfaces, Nat. Commun. 9 (1) (2018) 357.

[24] J. Grabarczyk, J. Gaj, B. Pazik, W. Kaczorowski, B. Januszewicz, Tribocorrosion behavior of Ti6Al4V alloy after thermo-chemical treatment and DLC deposition for biomedical applications, Tribol. Int. 153 (August 2020) (2021), https://doi.org/10.1016/j.triboint.2020.106560.

[25] C. Hu, D. Ashok, D.R. Nisbet, V. Gautam, Bioinspired surface modification of orthopedic implants for bone tissue engineering, Biomaterials 219 (June) (2019) 119366, https://doi.org/10.1016/j.biomaterials.2019.119366.

[26] B. Akhavan, S.G. Wise, M.M.M. Bilek, Substrate-regulated growth of plasma-polymerized films on carbide-forming metals, Langmuir 32 (42) (2016) 10835−10843.

[27] J. Peng, Y. Xiao, M. Yang, J. Liao, Effect of nitrogen doping on the microstructure and thermal stability of diamond-like carbon coatings containing silicon and oxygen, Surf. Coating. Technol. 421 (May) (2021) 127479, https://doi.org/10.1016/j.surfcoat.2021.127479.

[28] W. Yu, J. Wang, W. Huang, L. Cui, L. Wang, Improving high temperature tribological performances of Si doped diamond-like carbon by using W interlayer, Tribol. Int. 146 (January) (2020) 106241, https://doi.org/10.1016/j.triboint.2020.106241.

[29] K. Kyzioł, et al., Dual-purpose surface functionalization of Ti-6Al-7Nb involving oxygen plasma treatment and Si-DLC or chitosan-based coatings, Mater. Sci. Eng. C 121 (August 2020) 2021, https://doi.org/10.1016/j.msec.2020.111848.

[30] L. Liu, et al., Robust and durable surperhydrophobic F-DLC coating for anti-icing in aircrafts engineering, Surf. Coating. Technol. 404 (October) (2020) 126468, https://doi.org/10.1016/j.surfcoat.2020.126468.

[31] J.A. Santiago, et al., Tribomechanical properties of hard Cr-doped DLC coatings deposited by low-frequency HiPIMS, Surf. Coating. Technol. 382 (May 2019)

[32] (2020) 124899, https://doi.org/10.1016/j.surfcoat.2019.124899.

[32] H.-C. Hsueh, Y.-K. Wang, S. Lee, The effect of ammonia/acetylene ratio on characteristics of amorphous carbon films prepared by plasma enhanced chemical vapor deposition, Surf. Coating. Technol. 231 (2013) 353−356, https://doi.org/10.1016/j.surfcoat.2012.05.053.

[33] Y. Mabuchi, T. Higuchi, V. Weihnacht, Effect of sp2/sp3 bonding ratio and nitrogen content on friction properties of hydrogen-free DLC coatings, Tribol. Int. 62 (2013) 130−140, https://doi.org/10.1016/j.triboint.2013.02.007.

[34] S.C. Ray, W.F. Pong, P. Papakonstantinou, Iron, nitrogen and silicon doped diamond like carbon (DLC) thin films: a comparative study, Thin Solid Films 610 (2016) 42−47, https://doi.org/10.1016/j.tsf.2016.04.048.

[35] S. Bhattacherjee, H. Niakan, Q. Yang, Y. Hu, J. Dynes, Enhancement of adhesion and corrosion resistance of diamond-like carbon thin films on Ti-6Al-4V alloy by nitrogen doping and incorporation of nanodiamond particles, Surf. Coating. Technol. 284 (2015) 153−158, https://doi.org/10.1016/j.surfcoat.2015.08.072.

[36] D. Bootkul, B. Supsermpol, N. Saenphinit, C. Aramwit, S. Intarasiri, Nitrogen doping for adhesion improvement of DLC film deposited on Si substrate by Filtered Cathodic Vacuum Arc (FCVA) technique, Appl. Surf. Sci. 310 (2014) 284−292, https://doi.org/10.1016/j.apsusc.2014.03.059.

[37] A.D. Bakker, J. Klein-Nulend, "Osteoblast Isolation from Murine Calvaria and Long Bones," in *Bone Research Protocols*, Springer, 2012, pp. 19−29.

[38] J. Aveyard, et al., Linker-free covalent immobilization of nisin using atmospheric pressure plasma induced grafting, J. Mater. Chem. B 5 (13) (2017) 2500−2510, https://doi.org/10.1039/c7tb00113d.

[39] J. Cheng, et al., Triboelectric microplasma powered by mechanical stimuli, Nat. Commun. 9 (1) (2018) 1−11, https://doi.org/10.1038/s41467-018-06198-x.

[40] S. Ghafouri, et al., Study on physio-chemical properties of plasma polymerization in C2H2/N2 plasma and their impact on COL X, Sci. Rep. 7 (1) (2017) 1−16, https://doi.org/10.1038/s41598-017-09747-4.

[41] N. Bundaleska, et al., Large-scale synthesis of free-standing N-doped graphene using microwave plasma, Sci. Rep. 8 (1) (2018) 1−11, https://doi.org/10.1038/s41598-018-30870-3.

[42] C.A.C. Stewart, et al., Cellular responses to radical propagation from ion-implanted plasma polymer surfaces, Appl. Surf. Sci. 456 (2018) 701−710.

[43] C. John, Interpretation of infrared spectra, a practical approach, Encycl. Anal. Chem. 12 (2000) 10815−10837.

[44] S.E. Rodil, N.a. Morrison, J. Robertson, W.I. Milne, Nitrogen incorporation into tetrahedral hydrogenated amorphous carbon, Phys. Status Solidi 174 (1999) 25−37, https://doi.org/10.1002/(SICI)1521-396X(199907)174:1<25::AID-PSSA25>3.0.CO;2-3.

[45] F. Truica-marasescu, P. Girard-lauriault, A. Lippitz, W.E.S. Unger, M.R. Wertheimer, Nitrogen-rich plasma polymers : comparison of films deposited in atmospheric- and low-pressure plasmas 516 (2008) 7406−7417, https://doi.org/10.1016/j.tsf.2008.02.033.

[46] M. Lejeune, M. Benlahsen, P. Lemoine, Effect of air post contamination on mechanical properties of amorphous carbon nitride thin films, Solid State Commun. 135 (7) (2005) 434−439, https://doi.org/10.1016/j.ssc.2005.05.025.

[47] B. Akhavan, K. Jarvis, P. Majewski, Evolution of hydrophobicity in plasma polymerised 1, 7-O ctadiene films, Plasma Process. Polym. 10 (11) (2013) 1018−1029.

[48] B. Akhavan, K. Jarvis, P. Majewski, Tuning the hydrophobicity of plasma polymer coated silica particles, Powder Technol. 249 (2013) 403−411.

[49] T.D. Michl, et al., Plasma polymerization of 1,1,1-trichloroethane yields a coating with robust antibacterial surface properties, RSC Adv. 4 (52) (2014) 27604−27606, https://doi.org/10.1039/c4ra01892c.

[50] T.F. Zhang, K.-W. Kim, K.H. Kim, Nitrogen-incorporated hydrogenated amorphous carbon film electrodes on Ti substrates by hybrid deposition technique and annealing, J. Electrochem. Soc. 163 (3) (2016) E54−E61, https://doi.org/10.1149/2.0051603jes.

[51] J. Senthilnathan, C.C. Weng, J. Der Liao, M. Yoshimura, Submerged liquid plasma for the synthesis of unconventional nitrogen polymers, Sci. Rep. 3 (2013) 1−7, https://doi.org/10.1038/srep02414.

[52] S. Xu, S. Kumar, Y.A. Li, N. Jiang, S. Lee, Low-temperature synthesis of highly transparent carbon nitride thin films, J. Phys. Condens. Matter 12 (6) (2000), https://doi.org/10.1088/0953-8984/12/6/109.

[53] J. Ortiz-Medina, et al., Nanostructured carbon-based membranes: nitrogen doping effects on reverse osmosis performance, NPG Asia Mater. 8 (October 2015) (2016) 1−10, https://doi.org/10.1038/am.2016.27.

[54] K. Zhou, P. Ke, X. Li, Y. Zou, A. Wang, Microstructure and electrochemical properties of nitrogen-doped DLC films deposited by PECVD technique, Appl. Surf. Sci. 329 (2015) 281−286, https://doi.org/10.1016/j.apsusc.2014.12.162.

[55] X. Liu, R. Yamaguchi, N. Umehara, M. Murashima, T. Tokoroyama, Effect of oil temperature and counterpart material on the wear mechanism of ta-CNx coating under base oil lubrication, Wear 390−391 (August) (2017) 312−321, https://doi.org/10.1016/j.wear.2017.08.012.

[56] X. Liu, N. Umehara, T. Tokoroyama, M. Murashima, Tribological properties of

ta-CNx coating sliding against steel and sapphire in unlubricated condition, Tribol. Int. 131 (August 2018) (2019) 102−111, https://doi.org/10.1016/j.triboint.2018.10.022.

[57] C. Ronning, H. Feldermann, R. Merk, H. Hofsäss, P. Reinke, J.-U. Thiele, Carbon nitride deposited using energetic species: a review on XPS studies, Phys. Rev. B 58 (4) (1998) 2207−2215, https://doi.org/10.1103/PhysRevB.58.2207.

[58] Y.S. Zou, et al., Structural characterization of nitrogen doped diamond-like carbon films deposited by arc ion plating 241 (2005) 295−302, https://doi.org/10.1016/j.apsusc.2004.07.043.

[59] J. Friedrich, Mechanisms of plasma polymerization - reviewed from a chemical point of view, Plasma Process. Polym. 8 (9) (2011) 783−802, https://doi.org/10.1002/ppap.201100038.

[60] R.S. Neale, E. Gross, The chemistry of nitrogen radicals. VII. The abstraction of hydrogen from substituted toluenes by the piperidinium radical, J. Am. Chem. Soc. 89 (25) (1967) 6579−6583, https://doi.org/10.1021/ja01001a034.

[61] A. Badzian, T. Badzian, S.T. Lee, Synthesis of diamond from methane and nitrogen mixture, Appl. Phys. Lett. 62 (26) (1993) 3432−3434, https://doi.org/10.1063/1.109039.

[62] S. Lerouge, et al., Nitrogen-rich plasma polymer coatings for biomedical applications: stability, mechanical properties and adhesion under dry and wet conditions, Plasma Process. Polym. 12 (9) (2015) 882−895.

[63] S. Ohmagari, A. Power, Doping and Semiconductor Characterizations, 2018.

[64] R.N. Shimizu, N.R. Demarquette, Evaluation of surface energy of solid polymers using different models, J. Appl. Polym. Sci. 76 (12) (2000) 1831−1845.

[65] M.M.M. Bilek, D.R. McKenzie, A comprehensive model of stress generation and relief processes in thin films deposited with energetic ions, Surf. Coating. Technol. 200 (14−15) (2006) 4345−4354.

[66] B. Akhavan, B. Menges, R. Förch, Inhomogeneous growth of micrometer thick plasma polymerized films, Langmuir 32 (19) (2016) 4792−4799.

[67] J. Robertson, Diamond-like amorphous carbon, Mater. Sci. Eng. R Rep. 37 (4−6) (2002) 129−281.

[68] M. Ficek, et al., Ellipsometric investigation of nitrogen doped diamond thin films grown in microwave $CH_4/H_2/N_2$ plasma enhanced chemical vapor deposition, Appl. Phys. Lett. 108 (24) (2016) 2−7, https://doi.org/10.1063/1.4953779.

[69] A. Gharibyan, D. Hayrapetyan, Z. Panosyan, Y. Yengibaryan, Preparation of wide range refractive index diamond-like carbon films by means of plasma-enhanced chemical vapor deposition, Appl. Opt. 50 (31) (2011) G69−G73.

[70] A.K. Shukla, R. Balasubramaniam, Effect of surface treatment on electrochemical behavior of CP Ti, Ti-6Al-4V and Ti-13Nb-13Zr alloys in simulated human body fluid, Corrosion Sci. 48 (7) (2006) 1696−1720, https://doi.org/10.1016/j.corsci.2005.06.003.

[71] K. Vasilev, L. Britcher, A. Casanal, H.J. Griesser, Solvent-induced porosity in ultrathin amine plasma polymer coatings, J. Phys. Chem. B 112 (35) (2008) 10915−10921, https://doi.org/10.1021/jp803678w.

[72] J. Tomastik, R. Ctvrtlik, Nanoscratch test — a tool for evaluation of cohesive and adhesive properties of thin films and coatings, EPJ Web Conf. 48 (2013), https://doi.org/10.1051/epjconf/20134800027, 00027.

[73] B.D. Beake, A.J. Harris, T.W. Liskiewicz, Review of recent progress in nanoscratch testing, Tribol. Mater. Surface Interfac. 7 (2) (2013) 87−96, https://doi.org/10.1179/1751584X13Y.0000000037.

[74] M. Guerino, et al., The influence of nitrogen on the dielectric constant and surface hardness in diamond-like carbon (DLC) films, Diam. Relat. Mater. 13 (2) (2004) 316−319, https://doi.org/10.1016/j.diamond.2003.10.016.

[75] D. Hegemann, Controlling the nanostructure and stability of aC: H: N plasma polymers, Thin Solid Films 581 (2015) 2−6.

[76] T.R. Gengenbach, H.J. Griesser, Deposition Conditions Influence the Post-deposition Oxidation of Methyl Methacrylate Plasma Polymer films.Pdf, 1997, pp. 985−1000, no. October.

[77] J.C. Ruiz, A. St-Georges-Robillard, C. Thérésy, S. Lerouge, M.R. Wertheimer, Fabrication and characterisation of amine-rich organic thin films: focus on stability, Plasma Process. Polym. 7 (9−10) (2010) 737−753, https://doi.org/10.1002/ppap.201000042.

[78] T.R. Gengenbach, H.J. Griesser, Aging of 1, 3-diaminopropane plasma-deposited polymer films: mechanisms and reaction pathways, J. Polym. Sci. Part A Polym. Chem. 37 (13) (1999) 2191−2206.

[79] T.R. Gengenbach, Z.R. Vasic, R.C. Chatelier, H.J. Grlesser, A multi-technique study of the spontaneous oxidation of n-hexane plasma polymers 32 (1994) 1399−1414.

[80] J. Rodriguez-Hernandez, Wrinkled interfaces: taking advantage of surface instabilities to pattern polymer surfaces, Prog. Polym. Sci. 42 (2015) 1−41.

[81] R. Sipehia, G. Martucci, M. Barbarosie, C. Wu, Enhanced attachment and growth of human endothelial cells derived from umbilical veins on ammonia plasma modified surfaces of PTFE and ePTFE synthetic vascular graft biomaterials, Biomater. Artif. Cells Immobil. Biotechnol. 21 (4) (1993) 455−468.

[82] D.Y. Tseng, E.R. Edelman, Effects of amide and amine plasma-treated ePTFE vascular grafts on endothelial cell lining in an artificial circulatory system, J. Biomed. Mater. Res. An Off. J. Soc. Biomater. Japanese Soc. Biomater. Aust. Soc. Biomater. 42 (2) (1998) 188−198.

[83] P.A. Ramires, L. Mirenghi, A.R. Romano, F. Palumbo, G. Nicolardi, Plasma-treated PET surfaces improve the biocompatibility of human endothelial cells, J. Biomed. Mater. Res. An Off. J. Soc. Biomater. Japanese Soc. Biomater. Aust. Soc. Biomater. Korean Soc. Biomater. 51 (3) (2000) 535−539.

[84] H.J. Griesser, R.C. Chatelier, T.R. Gengenbach, G. Johnson, J.G. Steele, Growth of human cells on plasma polymers: putative role of amine and amide groups, J. Biomater. Sci. Polym. Ed. 5 (6) (1994) 531−554.

[85] R.K. Globus, S.B. Doty, J.C. Lull, E. Holmuhamedov, M.J. Humphries, C.H. Damsky, Fibronectin is a survival factor for differentiated osteoblasts, J. Cell Sci. 111 (10) (1998) 1385−1393.

[86] M. Hirota, H. Shimpo, C. Ohkubo, T. Umegaki, T. Toyama, T. Hayakawa, Bone adaptation of fibronectin-immobilized titanium implants using a tresyl chloride-activated method, J. Hard Tissue Biol. 24 (4) (2015) 341−346.

[87] A.M. Moursi, et al., Fibronectin regulates calvarial osteoblast differentiation, J. Cell Sci. 109 (6) (1996) 1369−1380.

[88] A.M. Moursi, R.K. Globus, C.H. Damsky, Interactions between integrin receptors and fibronectin are required for calvarial osteoblast differentiation in vitro, J. Cell Sci. 110 (18) (1997) 2187−2196.

[89] L.S. Shlyakhtenko, A.A. Gall, J.J. Weimer, D.D. Hawn, Y.L. Lyubchenko, Atomic force microscopy imaging of DNA covalently immobilized on a functionalized mica substrate, Biophys. J. 77 (1) (1999) 568−576.

[90] C.D. Hodneland, Y.-S. Lee, D.-H. Min, M. Mrksich, Selective immobilization of proteins to self-assembled monolayers presenting active site-directed capture ligands, Proc. Natl. Acad. Sci. Unit. States Am. 99 (8) (2002) 5048−5052.